INFORMATION TO USERS

This manuscript has been reproduced from the microfilm master. UMI films the text directly from the original or copy submitted. Thus, some thesis and dissertation copies are in typewriter face, while others may be from any type of computer printer.

The quality of this reproduction is dependent upon the quality of the copy submitted. Broken or indistinct print, colored or poor quality illustrations and photographs, print bleedthrough, substandard margins, and improper alignment can adversely affect reproduction.

In the unlikely event that the author did not send UMI a complete manuscript and there are missing pages, these will be noted. Also, if unauthorized copyright material had to be removed, a note will indicate the deletion.

Oversize materials (e.g., maps, drawings, charts) are reproduced by sectioning the original, beginning at the upper left-hand corner and continuing from left to right in equal sections with small overlaps. Each original is also photographed in one exposure and is included in reduced form at the back of the book.

Photographs included in the original manuscript have been reproduced xerographically in this copy. Higher quality 6" x 9" black and white photographic prints are available for any photographs or illustrations appearing in this copy for an additional charge. Contact UMI directly to order.

UMI

A Bell & Howell Information Company
300 North Zeeb Road, Ann Arbor MI 48106-1346 USA
313/761-4700 800/521-0600

Onset of Planetary Wave Breaking in a Model of the Polar Stratospheric Vortex

by

XIAOHONG WANG

M.Sc., University of Victoria, 1992
B.Sc., Jilin University, 1988

A Dissertation Submitted in Partial Fulfillment of the
Requirements for the Degree of

DOCTOR OF PHILOSOPHY

in the Department of Computer Science

We accept this dissertation as conforming
to the required standard

Dr. John Fyfe, Co-supervisor (School of Earth and Ocean Science)

Dr. Dale Olesky, Co-supervisor (Department of Computer Science)

Dr. Frank Roberts, Departmental Member (Department of Computer Science)

Dr. Andrew Weaver, Outside Member (School of Earth and Ocean Science)

Dr. Charles McLandress, External Examiner (University of Washington)

University of Victoria

Co-supervisors: Drs. John Fyfe and Dale Olesky

Abstract

The breakdown of vertically-propagating planetary waves in the stratosphere is investigated using an ultra-high horizontal resolution Contour Dynamics with Surgery model. In the model, planetary waves are forced at the tropopause and propagate upwards through the stratosphere and into an absorbing sponge (the first of its kind for such a model). In the context of wave breaking, two aspects of the system are questioned, namely, 1) what is the sensitivity to upper-boundary conditions? and 2) given perfect upper-boundary conditions what controls wave breaking?

1) In a Boussinesq environment, wave breaking is compared using: a) a rigid upper-boundary condition (as in previous work) and b) an absorbing sponge (preventing spurious reflections). In a) both local (to the forcing) and remote breaking is evidenced for weak forcing while only local breaking is observed for sufficiently strong forcing. In b) remote breaking is absent and local breaking, which occurs for sufficiently strong forcing, has quite a different character to that seen in a). Compressibility effects are also investigated.

2) A quasi-linear slowly-varying theory is developed which predicts wave breaking if the zonal mean flow decelerates by more than one-half of its initial value (via positive group-velocity/zonal-mean-flow feedbacks). This so-called "one-half" rule for planetary wave breaking is confirmed through fully-nonlinear simulations. Numerical simulations detail the precise sequence of events leading up to and after wave breaking.

Examiners:

Dr. John Fyfe, Co-supervisor (School of Earth and Ocean Science)

Dr. Dale Olesky, Co-supervisor (Department of Computer Science)

Dr. Frank Roberts, Departmental Member (Department of Computer Science)

Dr. Andrew Weaver, Outside Member (School of Earth and Ocean Science)

Dr. Charles McLandress, External Examiner (University of Washington)

Acknowledgements

First and foremost, I would like to express my deep gratitude to Dr. John Fyfe, my thesis supervisor, for his rigorous guidance on my doctoral research and invaluable help in this dissertation writing. His support throughout my Ph.D study is highly appreciated. I am also grateful to Dr. Dale Olesky, my departmental supervisor, for all his support and encouragement in the past few years. This dissertation is not possible without them.

My hearty thanks also go to the scientists and staff at Canadian Centre for Climate Modelling and Analysis. They have provided me with superb computing facilities as well as a friendly working environment. Dr. R. Saravanan from National Centre for Atmospheric Research kindly provided the Contour Dynamics with Surgery computer code as well as detailed help in the earlier stage of this research. I also benefited considerably from discussions with Dr. Ruping Mo from McGill University on some of the theoretical aspects of this dissertation.

Scholarship and other financial support from Department of Computer Science, University of Victoria, and Climate Research Network of the Atmospheric Research Service of Canada are gratefully acknowledged.

Last but not the least, I give my sincere thanks to my husband, Ming Li, for his love, patience, understanding and support.

To my parents

Contents

List of Figures

List of Tables

Chapter 1

Introduction

Planetary waves are the largest spatial scale waves on Earth. These waves, which are commonly seen in the Northern Hemisphere stratosphere, mostly owe their existence to surface forcing associated with large-scale topography and/or ocean-continent temperature contrasts (Charney and Eliassen, 1949; Derome and Wiin-Nielsen, 1971; Grose and Hoskins, 1979). Indeed, the fact that they are relatively weak in the Southern Hemisphere stratosphere [see Figure 1.1(b)[1]] as compared to the Northern Hemisphere stratosphere [see Figure 1.1(a)] is partly attributable to the obvious topographic asymmetries existing between the hemispheres.

The particular aspect of planetary waves which is of interest to us here is their ability to transport zonal mean momentum from the surface vertically, which when deposited aloft induces zonal mean circulation changes. Given that zonal mean vorticity gradients act as the restoring force for planetary waves, changes in the zonal mean circulation can in turn

---

[1] Note that figures for each chapter are located at the end of each chapter.

affect the propagation characteristics of the waves. In fact, under some circumstances these so-called "wave-mean" interactions can be rather extreme and lead to wave breakdown. Wave-mean interactions leading to wave breaking have been the subject of considerable research in the past (Andrews and McIntyre, 1976; Tung and Lindzen, 1979; Dunkerton, 1981; Fyfe and Held, 1990) and are the general topic of this dissertation.

Our primary interest here is in wave-mean interactions which lead to and/or promote planetary wave breaking. Like surface water waves approaching a beach, planetary waves are known to break as they propagate vertically through the middle atmosphere. However, unlike surface water waves the mechanisms underlying planetary wave breaking are less understood. Towards improving our understanding of planetary wave breaking we have set the following objectives for this study:

- To implement an ultra-high horizontal resolution mechanistic model of the stratosphere which incorporates an upper absorbing sponge. Ultra-high resolution is required to obtain accurate simulations of wave breaking, while an upper absorbing sponge is required to limit back reflections of vertically-propagating planetary waves.
- To develop a new analytical theory for the breakdown of vertically-propagating planetary waves which does not rely on the usual assumption of "critical levels" in the zonal mean flow. The theory will be tested, and where possible extended, through fully-nonlinear, ultra-high resolution simulations.

While the theory we will develop is fairly general in nature we will focus our attention on one specific application, namely, stratospheric sudden warmings. Stratospheric sudden warmings are one of the most striking examples of wave-mean interaction. Normally the winter stratosphere consists of an anticlockwise vortex centered on a cold polar cap [see Figure 1.1(a)]. The zonal mean zonal wind (i.e., east-west wind) is westerly (i.e., from the west) and the zonal mean temperature decreases towards the winter pole. However, during some winters the polar vortex is greatly disrupted within a few days (see Figure 1.2). During these episodes the polar stratospheric winds decrease rapidly with time and may even reverse from westerly to easterly. With this, the polar vortex breaks up and temperatures rise by tens of degrees. For obvious reasons such events are called stratospheric sudden warmings and it is generally accepted that the essential dynamical mechanism responsible for them involves the interaction of vertically-propagating planetary waves with stratospheric zonal mean flows (Andrews et al., 1987).

McIntyre and Palmer (1983) used meteorological analyses to show that planetary wave breaking is characteristic of the circumstances leading to stratospheric sudden warmings. This seminal observational paper spawned a number of ultra-high horizontal resolution modelling studies (Juckes and McIntyre, 1987; Juckes, 1989; Waugh, 1993; and Norton, 1994) to investigate the dynamics of planetary wave breaking, and specifically the effect of breaking on the erosion of the polar vortex. Horizontal resolution has been an important consideration in modelling studies since observations show that when the polar vortex breaks up, small-scales and sharp-gradients are rapidly generated over very localized regions (McIntyre and Palmer, 1983, 1984; Clough et al., 1985; Dunkerton and Delisi, 1986; Baldwin and Holton, 1988).

One of the first ultra-high resolution modelling studies of planetary wave breaking was that of Juckes and McIntyre (1987, hereafter JM). To solve the governing equations, JM used a "pseudo-spectral" numerical method which, as with other conventional methods, suffers from the computational disadvantage that uniform resolution is required over the whole domain even though, in this physical problem, wave activity is localized near the edge of the polar vortex. Here we will take a very different numerical approach to JM and solve the governing equations using the "Contour Dynamics with Surgery" method (hereafter CD/CS). The CD/CS method allows one to adapt the resolution to the problem at hand and so exploit the available computing resources much more fully.

"Contour Dynamics" was first proposed by Zabusky et al. (1979) and then extended by Dritschel (1988) to include a set of "surgical" procedures which effectively allow for infinite horizontal resolution. CD/CS is a Lagrangian method based on the recognition that in a conservative system the evolution of a patch of uniform vorticity is fully described by the behaviour of its bounding contour. In practice, this reduces the dimension of the physical problem in question by one, and in so doing greatly accelerates the computations. Of course, as the number of patches increases, so does the number of bounding contours and hence also the computational burden. Therefore best advantage of the method is realized in physical problems where a small number of patches (ideally one) is appropriate, such as the one at hand (Legras and Dritschel, 1993; Waugh, 1993).

The numerical model to be used here is the three-dimensional quasi-geostrophic CD/CS model developed by Dritschel and Saravanan (1994, hereafter DS). The main modification we have made to the model of DS (to be described in detail in Section 2.3) is the implementation of an absorbing sponge at the top of the model domain in order to limit back reflections of upward propagating waves (Lindzen et al., 1968; Beaudoin and Derome, 1976; Kirkwood and Derome, 1977). Such absorbing sponges are common in numerical models [e.g., the Canadian Middle Atmosphere Model (Beagley et al, 1997)] but are very difficult to incorporate in CD/CS models because of the conservation constraints that the techniques of CD/CS impose. Indeed, the absorbing sponge described in Section 2.3 is the first of its kind, and its design and implementation was the first major hurdle we needed to overcome to achieve our objectives. Preliminary results using the absorbing sponge were published in Fyfe and Wang (1997).

Now for a description of the key issue at the heart of this study. The main issue here involves explaining why planetary waves are often observed to break at heights lower than expected based on "critical level" theory (Barnett, 1975; Schoeberl, 1978). Critical level theory predicts that waves will break when their phase speed matches the speed of the zonal mean flow (Dickinson, 1970; Warn and Warn, 1976). For the special case of a topographically-forced stationary wave (i.e., with zero phase speed) a critical level occurs where the zonal mean flow is zero. However, as alluded to, stationary wave breaking is observed to occur in the absence of zero zonal mean flow, leading us to conclude that critical levels are not a necessary condition for wave breaking. Is there an explanation for the occurrence of stationary wave breaking in the absence of zero zonal mean winds?

Fyfe and Held (1990, hereafter FH) proposed a mechanism for Rossby wave breaking which predicts breaking under circumstances where there is no critical level (nor the expectation of one being generated given linear wave theory estimates). FH termed the main result of their theory the "two-fifths" rule for Rossby wave breaking (which will be discussed in detail in Chapter 4). While the two-fifths rule is powerful it is limited to horizontally-propagating Rossby waves and as such is not directly applicable to vertically-propagating planetary waves of the sort discussed here. It is our overall aim then to generalize the theory of FH to allow for an analysis of vertically-propagating planetary waves which are relevant to the stratosphere, and in particular, to the problem of stratospheric sudden warmings. Further to this we intend to exploit the power of our modified CD/CS model to simulate the detailed behaviour of wave breaking once initiated. FH used a pseudo-spectral numerical model, and as such were unable to characterize the breaking once it was initiated following the two-fifths rule.

The plan for this dissertation is as follows. In Chapter 2 we describe the governing equations and the CD/CS model used to solve them. In Chapter 3 we study the model sensitivity of planetary wave breaking to upper-boundary conditions. In Chapter 4 we present a new theory for the breakdown of vertically-propagating planetary waves and provide numerical simulations which verify the theory, and as well, show how the breaking waves behave outside the assumptions of the theory. In Chapter 5 we summarize the main results of this dissertation.

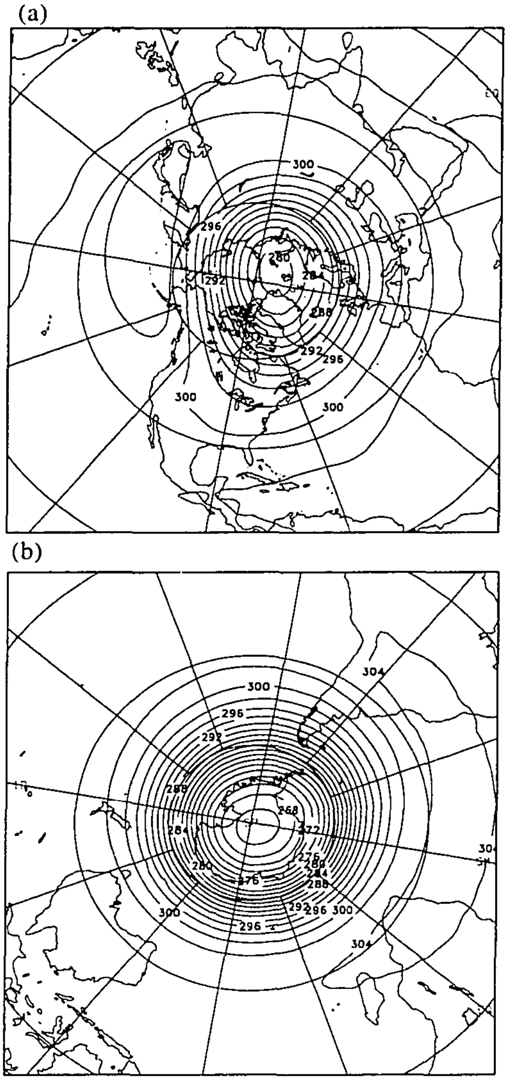

Figure 1.1: Geopotential at 10 mb for 1993-1997: (a) Dec-Jan-Feb mean for the Northern Hemisphere; (b) June-July-Aug mean for the Southern Hemisphere. Units are m^2s^{-2}. Data are from United Kingdom Meteorological Office (UKMO) analyses (Swinbank and O'Neill, 1994).

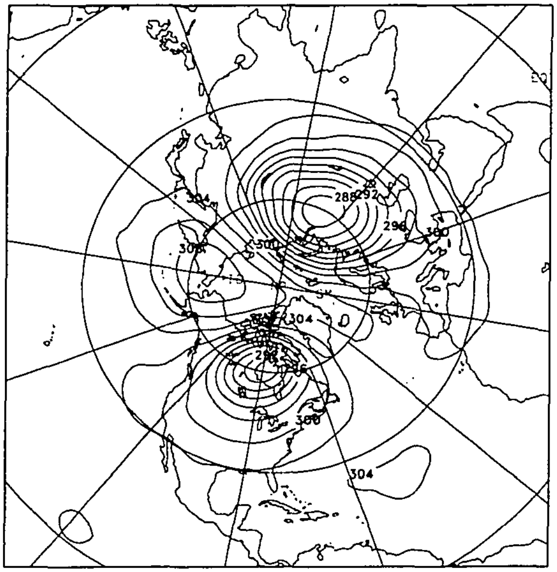

Figure 1.2: Geopotential at 10 mb for February 22, 1979 (00Z). Units are m^2s^{-2}. Data are from National Centre for Environmental Prediction (NCEP) reanalyses (Kalnay et al., 1996).

Chapter 2

The model

In this dissertation we employ a quasi-geostrophic potential vorticity (hereafter QG PV) model which except for one major modification (to be described in Section 2.3) is that of DS. This model approximately describes rapidly-rotating and strongly-stratified flow such as is seen in the extratropical stratosphere. In Sections 2.1, 2.2 and 2.3 we introduce the model's governing equations, PV discretization and initial/boundary conditions, respectively. In Section 2.4 we describe the numerical approach to solving the governing equations.

2.1 Governing equations

Assuming frictionless and adiabatic QG flow on an f-plane, the governing equation is

$$\frac{Dq}{Dt} \equiv \frac{\partial q}{\partial t} + \mathbf{u} \cdot \nabla q = 0 \tag{2.1}$$

(cf. Pedlosky, 1987). This equation states that QG PV q is conserved following the flow when advected by horizontal velocity $\mathbf{u}$, where

$$q = \nabla^2\psi + \frac{1}{\rho_\circ}\frac{\partial}{\partial z}\left(\frac{\rho_\circ}{B}\frac{\partial\psi}{\partial z}\right) \quad \text{and} \quad \mathbf{u} = \mathbf{k}\times\nabla\psi. \tag{2.2}$$

Here ∇ is the horizontal gradient vector, ψ the streamfunction and $\mathbf{k}$ the vertical unit vector. We use a log-pressure vertical coordinate z given by $z = H\ln(p_{\circ\circ}/p)$ where $H = RT_{\circ\circ}/g$ is the mean scale height (R being the ideal gas constant, $T_{\circ\circ}$ a constant reference temperature and g gravity acceleration), p pressure and $p_{\circ\circ}$ a constant reference pressure.

The reference density $\rho_\circ(z)$ and Burger number $B(z)$ are given by

$$\rho_\circ(z) = \rho_{\circ\circ}e^{-z/H} \quad \text{and} \quad B(z) = N_\circ^2(z)/f_\circ^2 \tag{2.3}$$

where $\rho_{\circ\circ}$ is a constant reference density, $f_\circ$=2Ω the constant Coriolis parameter (Ω being the angular rotation rate of Earth) and $N_\circ(z)$ the Brunt-Väisälä frequency given by $N_\circ^2(z) = (R/H)(d\theta_\circ/dz)e^{-\kappa z/H} = (R/H)(dT_\circ/dz + \kappa T_\circ/H)$ where $\theta_\circ(z) = T_\circ(z)e^{\kappa z/H}$ and $T_\circ(z)$ are the reference potential temperature and temperature, respectively (κ=R/c_p where c_p is specific heat capacity at constant pressure). In this dissertation we mainly consider a Boussinesq atmosphere, corresponding to taking $H \to \infty$ and $T_\circ = T_{\circ\circ}$. In this case $N_\circ^2 = (R/H)\kappa T_{\circ\circ}/H = g^2/c_pT_{\circ\circ}$ and

$$\rho_\circ = \rho_{\circ\circ} \quad \text{and} \quad B = \frac{g^2}{c_pT_{\circ\circ}f_\circ^2}. \tag{2.4}$$

This is a reasonable approximation to the real atmosphere when motions considered have small vertical wavelengths compared to the density scale height. In this dissertation we will mainly concentrate upon a Boussinesq atmosphere although some aspects of compressibility will be discussed in Section 3.4.

Values for the constants used in this dissertation are typical ones for the stratosphere, i.e., Ω=7.292×10^{-5} rads^{-1}; ρ_{oo}=1.225 kgm^{-3}; p_{oo}=101.3 kPa; T_{oo}=210 K; R=287 Jkg^{-1}K^{-1}; g=9.8 ms^{-2}; c_p=1012 JKg^{-1}K^{-1}. Derived constants are therefore set as $f_o \approx 1.458 \times 10^{-4}$ rads^{-1}, $\kappa \approx 2/7$ and $H \approx 6.14$ km.

In the polar-cap f-plane considered in this dissertation, the centre of the domain is at the North Pole and is unbounded horizontally (see Figure 2.1). As will be seen we will be working with the governing equations in either Cartesian [i.e., (x,y)] or polar cylindrical horizontal coordinates [i.e., (λ,r)].

Cartesian coordinates

In Cartesian coordinates **i** and **j** are unit vectors pointing in the x and y directions, respectively (see Figure 2.1). In this system the position and velocity vectors are given by $\mathbf{p} = x\mathbf{i} + y\mathbf{j}$ and $\mathbf{u} = u\mathbf{i} + v\mathbf{j}$, respectively, and the underlying equations take the form,

$$\frac{\partial q}{\partial t} + u\frac{\partial q}{\partial x} + v\frac{\partial q}{\partial y} = 0, \tag{2.5}$$

$$q = \frac{\partial^2 \psi}{\partial x^2} + \frac{\partial^2 \psi}{\partial y^2} + \frac{1}{\rho_o}\frac{\partial}{\partial z}\left(\frac{\rho_o}{B}\frac{\partial \psi}{\partial z}\right), \tag{2.6}$$

$$u = -\frac{\partial \psi}{\partial y} \quad \text{and} \quad v = \frac{\partial \psi}{\partial x}. \tag{2.7}$$

Polar cylindrical coordinates

In polar cylindrical coordinates **i** and **j** are unit vectors pointing in the λ (azimuthal) and r (radial) directions, respectively (see Figure 2.1). In what follows we use the terms azimuthal interchangeably with zonal and meridional interchangeably with radial. In this system the position and velocity vectors are given by $\mathbf{p} = \lambda\mathbf{i} + r\mathbf{j}$ and $\mathbf{u} = u\mathbf{i} + v\mathbf{j}$, respectively, and the underlying scalar equations take the form

$$\frac{\partial q}{\partial t} + \frac{u}{r}\frac{\partial q}{\partial \lambda} + v\frac{\partial q}{\partial r} = 0, \tag{2.8}$$

$$q = \frac{1}{r}\frac{\partial}{\partial r}\left(r\frac{\partial \psi}{\partial r}\right) + \frac{1}{r^2}\frac{\partial^2 \psi}{\partial \lambda^2} + \frac{1}{\rho_\circ}\frac{\partial}{\partial z}\left(\frac{\rho_\circ}{B}\frac{\partial \psi}{\partial z}\right), \tag{2.9}$$

$$u = \frac{\partial \psi}{\partial r} \quad \text{and} \quad v = -\frac{1}{r}\frac{\partial \psi}{\partial \lambda}. \tag{2.10}$$

Finally, we nondimensionalize the system with time scale $S = 4\pi/f_\circ = 1$ day; vertical length scale $H = RT_{\circ\circ}/g \approx 6.14$ km and horizontal length scale $L = N_\circ H/f_\circ \approx 902$ km. Thus we can define a horizontal velocity scale $U = L/S \approx 10.4$ ms^{-1}. Unless stated, variables other than those circumflexed are assumed nondimensional.

2.2 Piecewise-uniform potential vorticity

Our aim is to model the evolution of the polar stratospheric vortex subject to the disturbing influence of upward propagating planetary waves. To this end we assume that PV is simply piecewise-uniform, i.e., $q(z) = Q_i(z)$ inside the vortex edge $\mathcal{C}$ (see Figure 2.2) and $q(z) = Q_o(z)$ outside. r_e is the distance from the North Pole to a point at $\mathcal{C}$. The vortex edge evolves dynamically under the constraint that $Q_i(z)$ and $Q_o(z)$ is time-invariant. Hence $\Delta Q \equiv Q_i - Q_o$, which is the PV jump across the vortex edge, is also time-invariant. In general one might consider many such vortex edges (or equivalently many PV jumps) but in this dissertation we will, for computational reasons, consider only one such edge (or jump).

2.3 Initial and boundary conditions

Initial conditions

In this dissertation the system is initialized with a cylindrical PV column centered on the North Pole (shown in plan view Figure 2.1 by the bold circle centered on the North Pole). In mathematical terms this amounts to setting

$$r_e(\lambda, z, 0) = r_\circ \tag{2.11}$$

where $r_\circ$ is a constant. In all of the experiments discussed here we set $r_\circ = 3$. In general we could allow $r_\circ$ to vary as a function of z but for simplicity we choose not to. We note that in Chapter 3 we set Q_i and Q_o to constant values independent of height and in Chapter 4 we allow Q_i and Q_o to vary as a function of z.

Boundary conditions

The physical domain of the model is infinite horizontally but bounded vertically by rigid surfaces at the bottom z_B and top z_T of the domain. The top surface is flat while the bottom surface describes a large spatial scale topography of the form $R_\circ\eta$, where $R_\circ = U/(f_\circ L) \approx 0.08$ is the Rossby number and

$$\eta = \eta_\circ J_1\left(\frac{1.6}{r_\circ}r\right)T(r)S(t)\cos\lambda. \tag{2.12}$$

Here η_o is the non-dimensional topographic amplitude and J_1 a Bessel function. The taper-function

$$T(r) = \begin{cases} 1 & \text{for} \quad r \leq 5.0, \\ \cos\left(\dfrac{r-5.0}{5.0}\pi\right) & \text{for} \quad 5.0 < r < 7.5, \\ 0 & \text{for} \quad 7.5 \leq r, \end{cases} \tag{2.13}$$

sets the topography to zero at large r while the switch-on function,

$$\mathcal{S}(t) = \begin{cases} \sin^2\left(\dfrac{\pi t}{2t_s}\right) & \text{for} \quad 0 < t < t_s, \\ 1 & \text{for} \quad t_s \leq t, \end{cases} \tag{2.14}$$

allows the topography to be smoothly switched-on to its maximum value at time t_s. In Chapter 3 the topography is switched-on instantaneously [i.e., $\mathcal{S}(t) = 1$ for $t \geq 0$], while in Chapter 4, where we purposely attempt to generate a wave "front", the topography is switched-on slowly (with $t_s = 10$). A plot of the topography is shown in Figure 2.1 by the shaded contours. The mountain is identified with a "+" and the valley with a "-".

Since no flow can pass through a rigid surface one writes

$$\left.\frac{\partial\psi}{\partial z}\right|_{z=z_B} = -\frac{N_o^2}{f_o}\eta \quad \text{and} \quad \left.\frac{\partial\psi}{\partial z}\right|_{z=z_T} = 0. \tag{2.15}$$

Following DS, these troublesome nonhomogeneous boundary conditions can be replaced by homogeneous ones by introducing a modified streamfunction $\tilde{\psi}$,

$$\tilde{\psi} = \psi + \min(z, \sigma)\frac{N_o^2}{f_o}\eta \tag{2.16}$$

where σ is a small parameter ($\sigma \ll z_T$). Taking the z-derivative of $\tilde{\psi}$ yields

$$\left.\frac{\partial\tilde{\psi}}{\partial z}\right|_{z=z_B} = 0 \quad \text{and} \quad \left.\frac{\partial\tilde{\psi}}{\partial z}\right|_{z=z_T} = 0. \tag{2.17}$$

Further to this, ψ is replaced in Eq. (2.2) with $\tilde{\psi}$ to yield a modified q, i.e.,

$$q_{\text{tot}} \equiv q - f_{\text{o}}\eta\delta(z - z_B) = \nabla^2\tilde{\psi} + \frac{1}{\rho_{\text{o}}}\frac{\partial}{\partial z}\left(\frac{\rho_{\text{o}}}{B}\frac{\partial\tilde{\psi}}{\partial z}\right) \tag{2.18}$$

where δ is the Dirac delta function. Like q this modified QG PV satisfies

$$\frac{Dq_{\text{tot}}}{Dt} = 0. \tag{2.19}$$

Note that this is the equation to be solved in this dissertation.

Absorbing sponge

We now present the main modification we have made to the model of DS. To prevent back reflections of upward-propagating waves from the rigid top boundary we have implemented an absorbing sponge. Without such a sponge reflected waves would contaminate the interior flow and produce unrealistic results (as we shall demonstrate in Chapter 3). The description of the sponge we will now give is based on the assumption of a single patch of PV. The generalization to multiple patches is straightforward.

The sponge layer used here lies in the range $z_S \le z \le z_T$ where z_S is the bottom of the sponge. Over this range of heights the velocity $\mathbf{u}$ is adjusted in such a manner as to cause upward propagating waves to be damped, while at the same time maintaining temperatures near a prescribed and fixed profile. In this sense the sponge could be called a "Newtonian-cooling" sponge. To be more specific, the velocity field at any instant is adjusted in a "force-restore" manner, with forcing velocity $\mathbf{u}^f$ and restoring velocity $\mathbf{u}^r$, i.e.,

$$\mathbf{u}^s = \mathbf{u} + \mathbf{u}^f + \mathbf{u}^r \tag{2.20}$$

where $\mathbf{u}^s$ is the adjusted velocity. In the sponge, we choose

$$\mathbf{u}^f = \mu(z,t)\mathbf{k} \times \mathbf{u}^{bt} \quad \text{and} \quad \mathbf{u}^r = -\alpha(z)\frac{r}{2}\mathbf{j}$$

respectively where $\mathbf{u}^{bt}$ is the barotropic (i.e., height independent) component of $\mathbf{u}$.

The important point here is that both the forcing and restoring velocities are by design irrotational and as such neither introduces any external vorticity into the system. This is an important consideration because of the fact that our numerical approach to solving the underlying equations demands vorticity conservation (as we will see in the next subsection). Indeed, it is this constraint which until now has prevented the implementation of an absorbing sponge in such a CD/CS model.

The magnitude $\mu(z,t)$ of $\mathbf{u}^f$ is determined by solving (at each time step) the following equation [where $\int_{\mathcal{R}}()d\mathcal{R}'$ represents an area integral over area $\mathcal{R}$ enclosed by contour $\mathcal{C}$]

$$\int_{\mathcal{R}} (\mathbf{u}^r + \mathbf{u}^f) \cdot \nabla q_{\text{tot}} \, d\mathcal{R}' = \int_{\mathcal{R}} \frac{\alpha}{\rho_\circ} \frac{\partial}{\partial z} \left[\frac{\rho_\circ}{B} \frac{\partial}{\partial z} (\tilde{\psi} - \tilde{\psi}_e) \right] d\mathcal{R}', \tag{2.21}$$

where $\tilde{\psi}_e$ a prescribed equilibrium streamfunction which we take to be the initial state streamfunction and $\alpha(z)$ is a "Newtonian damping" coefficient defined as

$$\alpha(z) \quad = \quad \begin{cases} \alpha_T \times \{e^{-4\left(\frac{z - z_T}{z_T - z_S}\right)^2} - e^{-4}\} & \text{for} \quad z_S \leq z \leq z_T, \\ 0 & \text{for} \quad z < z_S, \end{cases} \tag{2.22}$$

where α_T is a constant which sets the maximum damping. In words, Eq. (2.21) equates the advection of q_{tot} by $\mathbf{u}^r + \mathbf{u}^f$ to the damping of vertical gradients of any temperature anomalies [i.e., $\partial(\tilde{\psi} - \tilde{\psi}_e)/\partial z$] that may arise in the sponge layer. In Eq. (2.22) we note that $\alpha[(z_T + z_S)/2] \approx \alpha_T e^{-1}$ and $\alpha(z_T) \approx \alpha_T$.

2.4 Numerics

The numerical approach used to solve the governing equations is the CD/CS method. The CD/CS method is a Lagrangian method which is based on the assumption that on level surfaces the PV (which is materially conserved) is initially, and for all time, piecewise-uniform. Out of this assumption comes the tremendous simplification that the evolution of the flow throughout the domain is solely determined by the movement of particles on contours separating regions of constant PV. We will now describe the method in detail for the special case of a single contour on each level surface.

We begin by vertically discretizing the system into N equally thick layers, allowing the modified streamfunction $\tilde{\psi}$ to be expanded as

$$\tilde{\psi}(\mathbf{x}, z, t) = \sum_{m=1}^{N} \chi_m(z)\varphi_m(\mathbf{x}, t) \tag{2.23}$$

where $\mathbf{x} = [x, y]$. Substituting $\chi_m(z)\varphi_m(\mathbf{x}, t)$ into Eq. (2.18) and letting q_{tot}=0 then leads to a Sturm-Liouville equation for the eigenfunction χ_m,

$$\frac{d}{dz}\left(\frac{\rho_o}{B}\frac{d\chi_m}{dz}\right) - \gamma_m^2 \rho_o \chi_m = 0 \qquad \text{with} \qquad \frac{d\chi_m}{dz} = 0 \quad \text{at } z = z_B, z_T. \tag{2.24}$$

Because B and ρ_o are positive, the eigenvalues γ_m^2 are guaranteed to be real, non-negative and ordered (cf. Boyce and DiPrima, 1986). Next we substitute Eq. (2.23) into Eq. (2.18) and make use of Eq. (2.24) to produce

$$\sum_{m=1}^{N} \left(\nabla^2 \varphi_m - \gamma_m^2 \varphi_m\right) \chi_m = q_{\text{tot}}, \tag{2.25}$$

which after multiplication by $\rho_o \chi_n$ (n is an integer between 1 and N) and vertical integration (note that the eigenfunctions χ_m are orthonormal) yields

$$\nabla^2\varphi_n - \gamma_n^2\varphi_n = \int_{z_B}^{z_T} \rho_o(z')\chi_n(z')q_{\text{tot}}(\mathbf{x}, z', t)dz'. \tag{2.26}$$

φ_n is obtained by inverting the above equation using the Green's function of the Helmholtz operator. Putting the φ_n back into Eq. (2.23) gives

$$\tilde{\psi}(\mathbf{x}, z, t) = \int_{\mathcal{R}} \left[\int_{z_B}^{z_T} \rho_o(z')q_{\text{tot}}(\mathbf{x}', z', t)G(\mathbf{x}, z; \mathbf{x}', z')dz' \right] d\mathcal{R}', \tag{2.27}$$

with Green's function

$$G(\mathbf{x}, z; \mathbf{x}', z') = -\frac{1}{2\pi}\sum_{m=1}^{N} \chi_m(z)\chi_m(z')K_o\left(\gamma_m|\mathbf{x}' - \mathbf{x}|\right) \tag{2.28}$$

where K_o is the modified Bessel function. Making use of Eq. (2.7) we have

$$\mathbf{u} = \int_{z_B}^{z_T} \rho_o(z') \left[\int_{\mathcal{R}} \left\{ [\partial_{y'}, -\partial_{x'}]G(\mathbf{x}, z; \mathbf{x}', z') \right\} q_{\text{tot}}(\mathbf{x}', z', t)d\mathcal{R}' \right] dz',$$

which after using Green's theorem leads to

$$\mathbf{u} = -\int_{z_B}^{z_T} \rho_o(z')\Delta Q(z') \left\{ \oint_C G(\mathbf{x}, z; \mathbf{x}', z')[dx', dy'] \right\} dz' \tag{2.29}$$

where $\Delta Q(z) = Q_i(z) - Q_o(z)$. In this crucial step the velocity determination reduces from an area integral to a line integral, thereby reducing the dimension of the problem by one. The next crucial step follows from Kelvin's circulation theorem which states that fluid particles on a material line remain on that line forever (cf. Kundu, 1990). Since the bounding contour C is a material line, the contour movement can be tracked by following the individual particles making up the contour, and from the contour position the velocity field can be obtained anywhere in the domain using Eq. (2.29).

To evaluate Eq. (2.29) we discretize the bounding contour $\mathcal{C}$ into a finite number of nodes connected by cubic spline line segments. The line integral in Eq. (2.29) can be calculated by adding the line integrals along all the cubic spline lines connecting the nodes on $\mathcal{C}$. Given the horizontal location vector of a node $\mathbf{x}$ and corresponding horizontal velocity vector $\mathbf{u}$ at level z and time t, we can calculate its subsequent location by evaluating

$$\frac{d\mathbf{x}}{dt} = \mathbf{u}(\mathbf{x}, z, t).$$

This equation consists of a system of coupled ordinary differential equations which are solved using a fourth-order Runge-Kutta scheme to achieve high-order temporal accuracy.

An important feature of the CD/CS method is that it is adaptive (Zabusky and Overman, 1983). As a contour deforms under its self-generated velocity field, the number of nodes and their location are adjusted where and when necessary to maintain an adequate resolution everywhere along the contour. For example, additional nodes are often inserted and rearranged together with existing nodes in regions of increasing curvature. Nodes may also be removed from regions where the curvature is weakening. These operations are performed (or not) on the basis of a computed local density, which is determined mainly by the local curvature and the presence of nearby small spatial scale features. A formula for calculating the local density at each nodal point has been obtained empirically (Dritschel, 1989).

The adaptive procedure is appealing but limited. As contours become increasingly complex (as they often will) adaptation quickly becomes prohibitively expensive [increasing as the square of the number of nodes, Dritschel (1988)]. To overcome this limitation various "surgical" operations have been introduced (Dritschel, 1988) which automatically remove features smaller than a predefined so-called surgical scale δ_s (set to 0.00125 in this dissertation). Contour surgery consists of two operations: 1) labelling and subsequent removal of corners and 2) separation and reconnection of contours. 1) If the curvature at a node exceeds δ_s^{-1}, the node is connected to its neighbours with straight lines nearly forming an acute angle, then the node is labelled as a corner. In this special case the curvature of the node and its two neighbours are set to zero so that no additional nodes are added in the vicinity during the adaptation stage of the computation. However, when the angle made by the line segments connecting the corner and its neighbours becomes obtuse, the node loses its corner status and the adaptive procedures resume for this node as for any other ordinary node. 2) When two parts of a contour approach each other by a distance less than δ_s, they are separated into two closed contours. On the other hand, when parts of two closed contours approach each other by a distance less than δ_s, they are connected as a single contour. In addition, the ends of excessively thin contours (sometimes called filaments) consisting of five or less nodes are permanently removed.

Surgery allows CD/CS calculations to extend well beyond the conventional CD method and thereby allows for exceedingly complex vorticity dynamics to evolve. The underlying assumption of surgery is that scales smaller than the predefined scale δ_s are dynamically insignificant and will not grow with time.

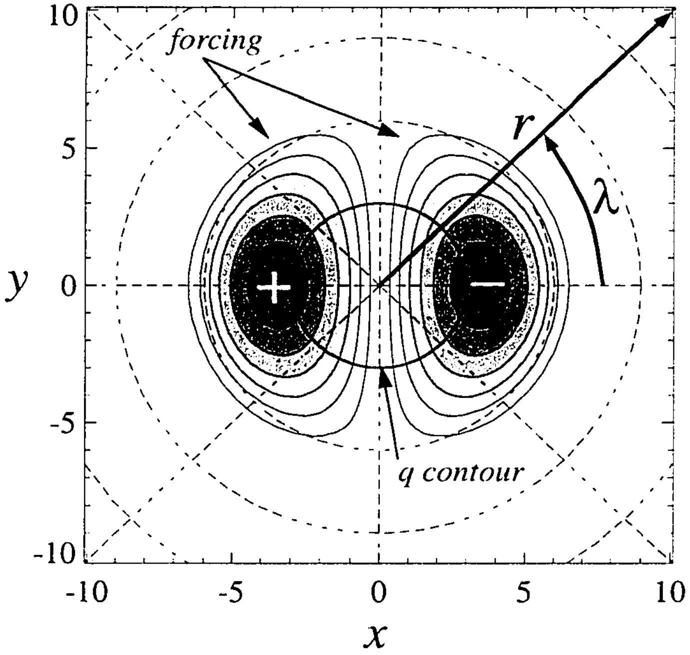

Figure 2.1: Plan view of the initial polar vortex (bold circle) on an f-cap plane. The topography is shown by shaded contours. The North Pole is the centre of the plot.

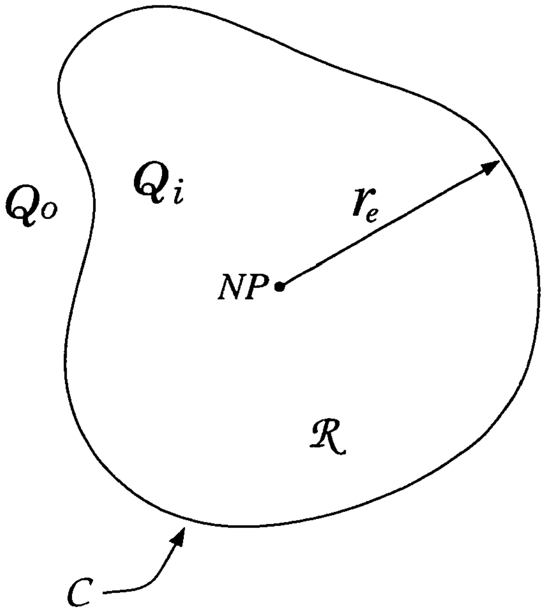

Figure 2.2: A single patch vortex with interior and exterior vorticity Q_i and Q_o, respectively. $\mathcal{C}$ is the bounding contour and the area enclosed by $\mathcal{C}$ is $\mathcal{R}$. r_e is the distance from the North Pole to $\mathcal{C}$. NP denotes the North Pole.

Chapter 3

Upper-boundary effects on planetary wave breaking

In this Chapter we describe a series of experiments designed to assess the effects of upper boundaries on planetary wave breaking. DS studied the response of an initially barotropic vortex to topographic forcing of varying amplitude in the presence of a rigid lid. The main result of DS was that for either Boussinesq or compressible flow two regimes of wave breaking exist, namely, 1) local breaking near the lower boundary at strong forcing or 2) remote breaking near the lid at weak forcing. 1) Local wave breaking, which is directly topographically forced, is insensitive to the upper-boundary condition and has an apparent shielding effect on upward wave propagation. 2) Remote wave breaking, which involves vertical transport of wave activity, is sensitive to the upper boundary condition and is coupled with the compressibility effect when compressibility is invoked. It is the upper-boundary condition sensitivities that we shall investigate by placing our Newtonian-cooling sponge under the model's rigid lid. To this end we will mainly focus on Boussinesq flow in order to isolate upper-boundary effects when those effects are important. Towards the end of the Chapter we will investigate how the compressibility effect modifies our conclusions. We again note that most of the results of this Chapter were published in Fyfe and Wang (1997).

The plan for this chapter is as follows. Section 3.1 describes the model setup, Section 3.2 the sponge parameter sensitivity experiments and Section 3.3 the wave breaking experiments. In Section 3.4 we summarize the Boussinesq results and how they are modified by the compressibility effect.

3.1 Model setup

The general model setup was described in Chapter 2. Here we introduce some features of the model specific to this Chapter. Here the bottom of the domain is fixed at $\hat{z}_B = 12$ km (nominally the tropopause) while the top of the domain $\hat{z}_T$ ranges from about 48 to 144 km (depending on the particular experiment). Numerical solutions are obtained using a layer thickness of about 2.4 km, which depending on $\hat{z}_T$ yields 20 to 66 layers. The model is initialized with a cylindrical PV column with radius $r_o = 3$ and with $Q_i = 5.2\pi$ and $Q_o = 3.6\pi$. The column is disturbed topographically with an instantaneously switched-on forcing (Figure 2.1). The instantaneously switched-on forcing enables us to compare our results with those of DS. Note that Q_i, Q_o and r_o are all independent of height in this Chapter. In the experiments with the absorbing sponge the bottom of the sponge layer is at $\hat{z}_S = 48$ km.

3.2 Vertical sponge sensitivity experiments

The vertical sponge thickness, $\hat{z}_T - \hat{z}_S$ and maximum relaxation rate α_T (quoted in Section 2.3) have been determined by trial and error using a vertical sponge under a weak forcing condition (i.e., $\eta_o = 0.15$). The rationale for the weak forcing, at this stage, is that since there is no wave breaking (and the response is nearly linear) the simulations are relatively easy to interpret and economical. Consider Figure 3.1, which for a range of relaxation rates shows the total wave activity density (hereafter total wave activity) when $\hat{z}_T = 120$ km (giving about a twelve scale height vertical sponge). Wave activity is a useful diagnostic for monitoring the mean-square amplitude of wave disturbances relative to a circularly symmetric basic flow (see Appendix A for a full definition of wave activity). In the $\alpha_T = 0.0$ (no vertical sponge) simulation we see initial upward wave propagation which after apparent multiple boundary reflections leads to a complicated and unsteady vertical structure. On the other hand, when $1.6 \leq \alpha_T \leq 3.2$, the boundary reflections are largely brought under control. As seen in Figure 3.2, dropping the top of the vertical sponge to $\hat{z}_T = 72$ km (giving about a four scale height thickness and a much reduced computational load) does not seriously compromise the absorbing ability of the vertical sponge. It is on the basis of these experiments, and others with larger topographic amplitudes (see Table 3.1 for a summary of all experiments conducted), that we have selected $\hat{z}_T = 72$ km and $\alpha_T = 1.6$ as our main vertical sponge parameters.

3.3 Main experimental results

Consider Table 3.1 which summarizes the various experiments conducted (over 45 in total). The main set of experiments to be discussed (in bold type in Table 3.1) build upon the Boussinesq rigid upper-boundary experiments of DS, where $\eta_o = 0.45$ or $\eta_o = 0.60$. The plan here is to contrast wave breaking seen with and without a vertical sponge.

3.3.1 Rigid upper boundary

Here we consider two sets of experiments: rigid upper boundary at 1) $\hat{z}_T = 48$ km (low rigid upper boundary) and 2) $\hat{z}_T = 72$ km (high rigid upper boundary). In subsequent subsections we introduce a vertical sponge in the region 48 km $\leq \hat{z} \leq$ 72 km, and so in a sense the present experiments can be considered as limiting vertical sponge cases with 1) corresponding to $\alpha_T \to \infty$ and 2) corresponding to $\alpha_T \to 0$.

Low rigid upper boundary

Consider Figure 3.3(a) and (b) which show perspective views of a weakly forced (hereafter $\mathcal{BL}_{0.45}$, $\mathcal{BL}$ standing for "Boussinesq low rigid upper boundary") and strongly forced (hereafter $\mathcal{BL}_{0.60}$) vortex, respectively. These are DS's $\mathcal{B}4$ and $\mathcal{B}6$ experiments respectively, using their nomenclature. To $t = 5$ the $\mathcal{BL}_{0.45}$ and $\mathcal{BL}_{0.60}$ vortices are very similar with the lower (upper) contours moving southward in the positive y direction (x direction). At $t = 10$ (not shown) lower-level breaking has just begun in the $\mathcal{BL}_{0.45}$ simulation but is quite advanced in the $\mathcal{BL}_{0.60}$ simulation. By $t = 15$ upper-level contour deformations dominate the $\mathcal{BL}_{0.45}$ simulation while lower-level breaking dominates the $\mathcal{BL}_{0.60}$ simu-

Table 3.1: Summary of Boussinesq experiments performed, where $\hat{z}_T$ is the dimensional domain height (km), α_T the relaxation rate (where applicable) and η_o is the topographic amplitude. The main set of experiments to be discussed are in bold-type and the identifying labels are in parentheses.

Upper boundary	$\hat{z}_T$ (km)	α_T		
		$\eta_o = 0.15$	$\eta_o = 0.45$	$\eta_o = 0.60$
Rigid Lid	48	0.0	**0.0** ($\mathcal{BL}_{\mathbf{0.45}}$)	**0.0** ($\mathcal{BL}_{\mathbf{0.60}}$)
	60	0.0	0.0	0.0
	72	0.0	**0.0** ($\mathcal{BH}_{\mathbf{0.45}}$)	**0.0** ($\mathcal{BH}_{\mathbf{0.60}}$)
	96	0.0	-	-
	120	0.0	-	-
	144	0.0	-	-
Vertical Sponge	60	0.8, 1.2, 1.6	0.8, 1.2, 1.6	0.8, 1.2, 1.6
	72	0.4, 0.8, 1.2, 1.6 2.0, 2.4, 2.8, 3.2	0.8, 1.2 **1.6** ($\mathcal{BS}_{\mathbf{0.45}}$), 2.8	0.8, 1.2 **1.6** ($\mathcal{BS}_{\mathbf{0.60}}$), 2.8
	96	1.6	-	-
	120	0.4, 0.8, 1.2, 1.6 2.0, 2.4, 2.8, 3.2	-	-

lation. At $t = 15$, the upper-level contours in the $\mathcal{BL}_{0.45}$ simulation are stretched way out [see the plan view of the top contour (dotted) in Figure 3.4(a)] while the lower-level contours are filamented [see the plan view of the bottom contour (solid) in Figure 3.4(a)]. At $t = 15$ the upper-level contours in the $\mathcal{BL}_{0.60}$ simulation are relatively quiescent [see the plan view of the top contour (dotted) in Figure 3.4(b)] while the lower-level contours are broken and dramatically deformed [see the plan view of the bottom contour (solid) in Figure 3.4(b)]. Here, the strong lower-level breaking evidently shields the upper-level contours from the dramatic deformations seen in the corresponding $\mathcal{BL}_{0.45}$ contours (as suggested by DS). A physical reason is that the low level breaking homogenizes the PV, which in effect removes the restoring force needed for the vertical propagation of planetary waves. Our vertical sponge experiments to come will show which aspects of this picture are artifacts of the rigid upper boundary and which are not.

Another way to look at these simulations is through height-time cross sections of total and relative wave activity (Figure 3.5). Relative wave activity is the component of the total wave activity which is due to motions relative to the centroid of the vortex, i.e., motions that leads to the shape changes of the vortex. In either the $\mathcal{BL}_{0.45}$ or $\mathcal{BL}_{0.60}$ cases we see an accumulation of the total wave activity at the top of the domain up to $t \approx 5$. It is during this time that the vortex obtains its strong tilt with height as the upper-level contours shift off the Pole in the direction of low topographic heights (see Figure 2.1). At $t \approx 10$ the total wave activity again builds, mostly at upper levels in the $\mathcal{BL}_{0.45}$ simulation and at lower levels in the $\mathcal{BL}_{0.60}$ simulation (further evidence of the shielding effect alluded to in the last paragraph). The relative wave activity plots indicate that these behaviours are due to contour shape changes as much as they are to changes in the position of the centroid of the vortex. We also note the impression of waves reflecting downwards from the top at $t \approx 5$ (the maxima of total wave activity at the top around that time), reaching the bottom at $t \approx 10$ (the maxima of total wave activity at the bottom around that time) and then in the $\mathcal{BL}_{0.45}$ simulation reflecting upwards to cause the subsequent upper-level havoc and in the $\mathcal{BL}_{0.60}$ case setting off the dramatic lower-level breaking (and perhaps suppressing further wave propagation as suggested by DS). Further diagnostics would be required to confirm these hypothesized chains of events.

High rigid upper boundary

How does the picture change when the rigid upper boundary is lifted to $\hat{z}_T = 72$ km? Consider Figures 3.6(a) and (b) which are the perspective views of a weakly forced (hereafter $\mathcal{BH}_{0.45}$, where $\mathcal{H}$ stands for high rigid upper boundary) and strongly forced (hereafter $\mathcal{BH}_{0.60}$) vortex, respectively, when $\hat{z}_T = 72$ km. Nothing appreciably different from the low upper boundary case happens to the vortex before $t \approx 5$, whether weakly or strongly forced. After $t \approx 5$ the $\mathcal{BH}_{0.60}$ vortex evolves much as the $\mathcal{BL}_{0.60}$ one, in the sense that the breaking is confined to the lower half of the domain and is very complex, [i.e., involving vortex displacement, reshaping, filamentation and secondary development (compare Figure 3.7(b) and Figure 3.4(b) solid curves)]. On the other hand, after $t \approx 5$ the $\mathcal{BH}_{0.45}$ vortex evolves much differently than the $\mathcal{BL}_{0.45}$ case insofar as the former's upper-level contours undergo relatively little shape change [compare Figure 3.7(a) and Figure 3.4(a), dashed curves]. We note in the $\mathcal{BH}_{0.45}$ case subsequent to $t \approx 15$ (not shown), two distinct regions of breaking develop, one near a kink in the vortex at $z \approx 7.5$ and another near the bottom. An early hint of this behaviour is seen in the bottom left panel of Figure 3.8 which shows relative wave activity maxima at $z \approx 7.5$ and $z \approx z_B$ beginning around $t = 10$.

3.3.2 Vertical sponge

Let us now consider placing a vertical sponge in the region 48 km $\leq \hat{z} \leq$ 72 km. Comparing Figure 3.9 and Figure 3.6 there appears little difference between the $\mathcal{BH}$ (high rigid upper boundary) and the $\mathcal{BS}$ (vertical sponge) cases up to $t \approx 5$ (i.e., with or without a vertical sponge the vortex is tilted with height and there is some minor lower-level breaking when strongly forced). Beyond $t \approx 5$ the evolution is quite different. For example, the $\mathcal{BS}_{0.45}$ vortex [Figure 3.9(a) and Figure 3.10(a)] remains in a more or less steady state (except for some relatively minor lower-level breaking) to $t \approx 15$ (and in fact to the end of the simulation at $t = 25$, not shown). On the other hand, the corresponding $\mathcal{BH}_{0.45}$ vortex [Figure 3.6(a) and Figure 3.7(a)] shows advanced breaking and/or contour distortion throughout the lower two-thirds of the domain during the same time. The $\mathcal{BS}_{0.60}$ [Figure 3.9(b) and Figure 3.10(b)] and $\mathcal{BH}_{0.60}$ [Figure 3.6(b) and Figure 3.7(b)] simulations are also quite different. Although both simulations exhibit significant lower-level breaking, the character of the breaking is quite different. Specifically, the $\mathcal{BS}_{0.60}$ vortex remains more or less intact despite winding and then expulsion of a thin and seemingly passive filament. The $\mathcal{BH}_{0.60}$ vortex, on the other hand, shows a much less recognizable main vortex and the development of a secondary vortex. For completeness we show the $\mathcal{BS}$ wave activity plots in Figure 3.11, which when compared to the corresponding $\mathcal{BH}$ plots in Figure 3.8, further punctuates our point that the evolution of a barotropic vortex can be highly sensitive to the upper-boundary condition.

3.4 Discussion

The study in this Chapter was primarily motivated by DS who used a three-dimensional QG CD/CS numerical model to study the response of a barotropic vortex to topographic forcing of varying amplitude. Our specific question, in the context of DS, is what is the role of the rigid upper-boundary condition in wave breaking? We have addressed this question by placing a vertical sponge under the rigid upper boundary. Our main results are:

- Given a vertical sponge and a forcing amplitude greater than a certain critical value, breaking is as in the corresponding rigid upper boundary case insofar as it is confined to the lower half of the vortex. However, important differences exist. For example, with a vertical sponge the vortex remains fairly true to its initial circular shape but is wrapped by a long narrow filament at lower levels. Without a vertical sponge the vortex is so deformed at lower levels as to be nearly unrecognizable.

- Given a vertical sponge and a forcing amplitude less than the critical value no breaking exists. This contrasts with the rigid upper boundary case which shows significant deformations near the upper boundary. Evidently the upper-level deformations are an artifact of the rigid upper-boundary condition.

Our conclusions so far are based on the assumption of a constant density profile. Now we consider an isothermal (i.e., $T_\circ = 210\mathrm{K}$) atmosphere in which the density $\rho_\circ$ has an exponential profile given as Eq. (2.3). The degree to which our Boussinesq results hold will depend upon the point at which wave amplitudes become large enough, due to the density effect, to break. If that point is situated well above the model domain then our Boussinesq results should hold to first approximation. If, on the other hand, that point lies within the model domain our conclusions will have to be modified. For example, Figure 3.12(a)-(c) show a series of experiments ($\mathcal{CL}_{0.15}$, $\mathcal{CL}_{0.175}$ and $\mathcal{CL}_{0.25}$ where $\mathcal{C}$ stands for "compressible") with an exponential density profile and a rigid lid located just above the top-most contour (as considered in DS). To judge whether or not the upper-level breaking is due to the density effect (i.e., wave amplitudes increasing exponentially with height) or the rigid-lid effect (discussed earlier) we repeat this set of simulations but with our absorbing sponge replacing DS's rigid lid [see Figure 3.12(d)-(f)]. Given the close correspondence between the rigid-lid and absorbing sponge simulations we conclude that for this range of forcing amplitudes the density effect dominates the upper-level response, with upper-boundary condition playing only a minor role (consider also Figure 3.13 for the corresponding plan views). Further in this vein, consider Figure 3.14 where, given a much reduced topographic amplitude (i.e., $\eta_\circ = 0.04$), we contrast low rigid-lid $\mathcal{CL}_{0.04}$, high rigid-lid $\mathcal{CH}_{0.04}$ and absorbing sponge $\mathcal{CS}_{0.04}$ simulations. For this topographic forcing it appears that the density effect only becomes significant within the region of sponge as shown in Figure 3.14(b). The upper-level breaking seen in the low rigid-lid experiment is therefore interpreted as a local amplification due to boundary reflections (as in our small amplitude Boussinesq simulations).

In this Chapter we have studied upper-boundary effects on planetary wave breaking. To eliminate spurious reflections from the top boundary, we have developed and tested a Newtonian cooling sponge layer. Using the CD/CS model with this sponge layer, we now investigate the dynamics leading to planetary wave breaking.

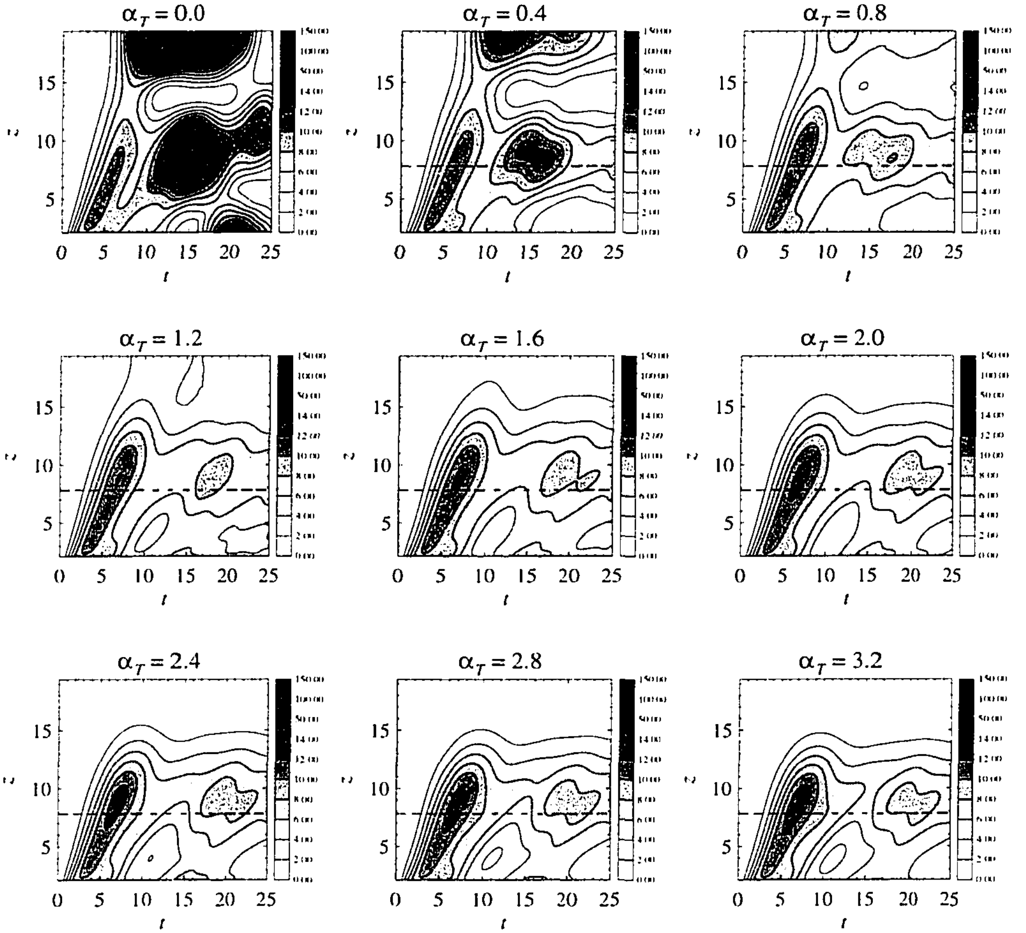

Figure 3.1: Total wave activity density normalized by η_o^2 for a range of relaxation rates α_T with $\hat{z}_T$=120km (i.e., z_T=19.5) and η_o=0.15. Where applicable the vertical sponge bottom is indicated by a horizontal dashed line. Note the nonlinear wave activity scale.

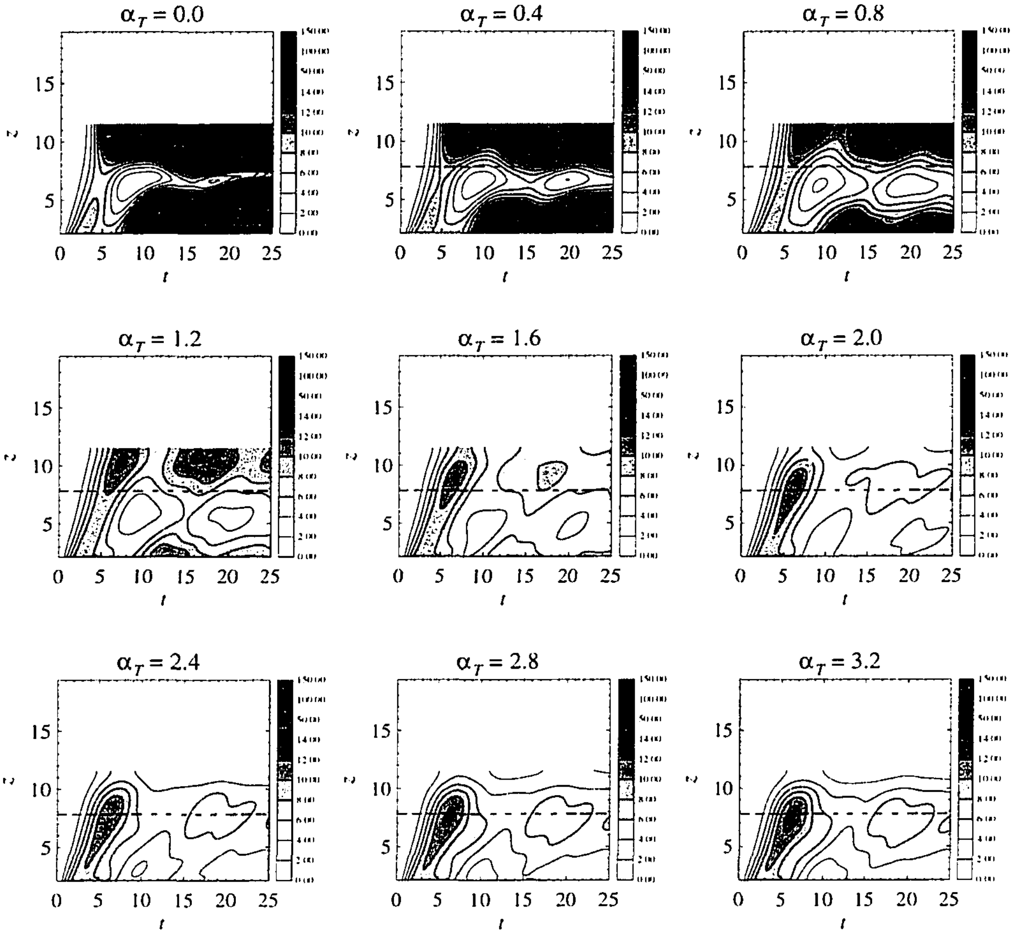

Figure 3.2: As in Figure 3.1 but for $\hat{z}_T$=72km (i.e., z_T=11.7).

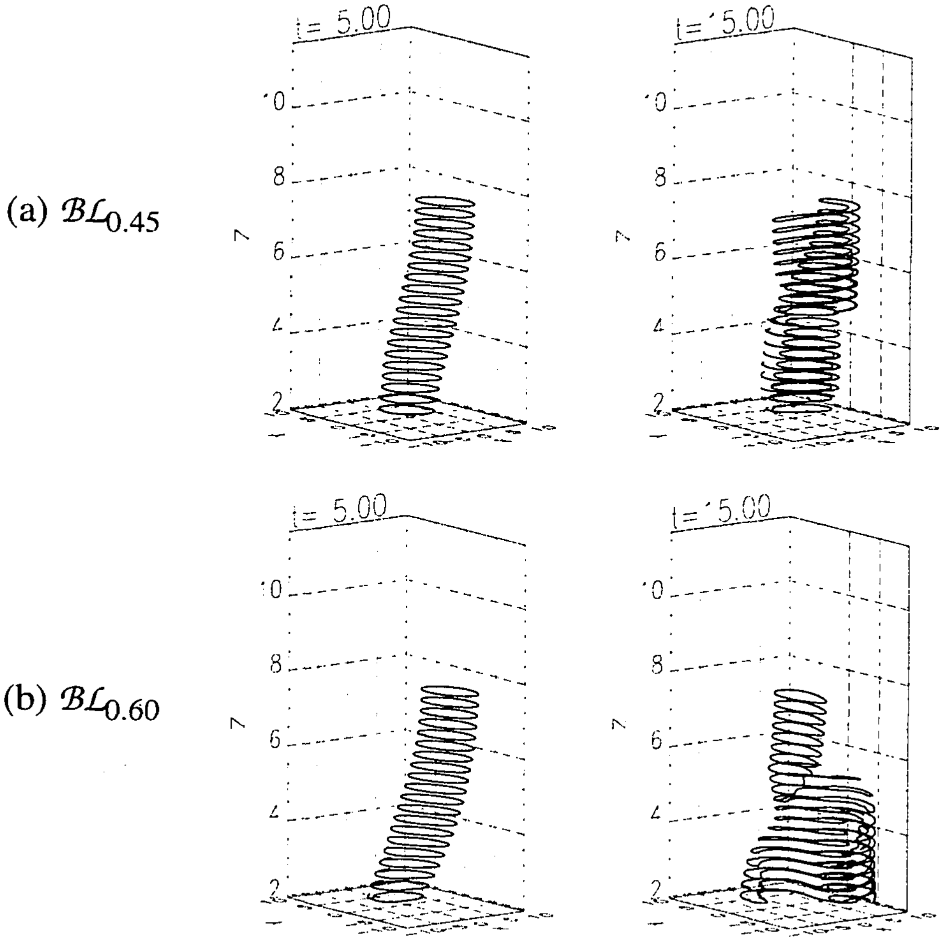

Figure 3.3: Perspective views of the vortex for the case of a low rigid upper boundary: (a) $\mathcal{BL}_{0.45}$ (η_o=0.45); (b) $\mathcal{BL}_{0.60}$ (η_o=0.60).

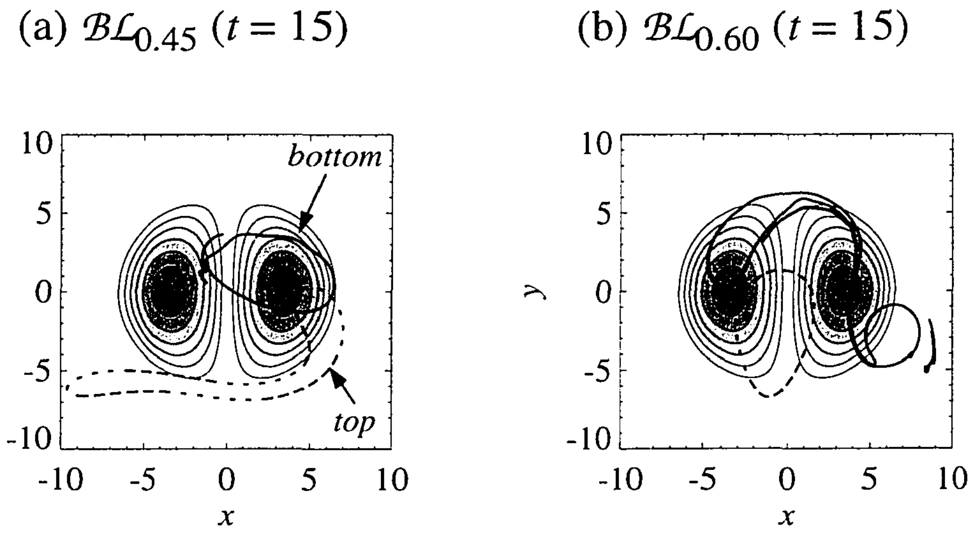

Figure 3.4: Top level (dotted) and bottom level (solid) potential vorticity contours for the case of a low rigid upper boundary: (a) $\mathcal{BL}_{0.45}$ (η_o=0.45); (b) $\mathcal{BL}_{0.60}$ (η_o=0.60). The bottom topography is shown by shaded contours.

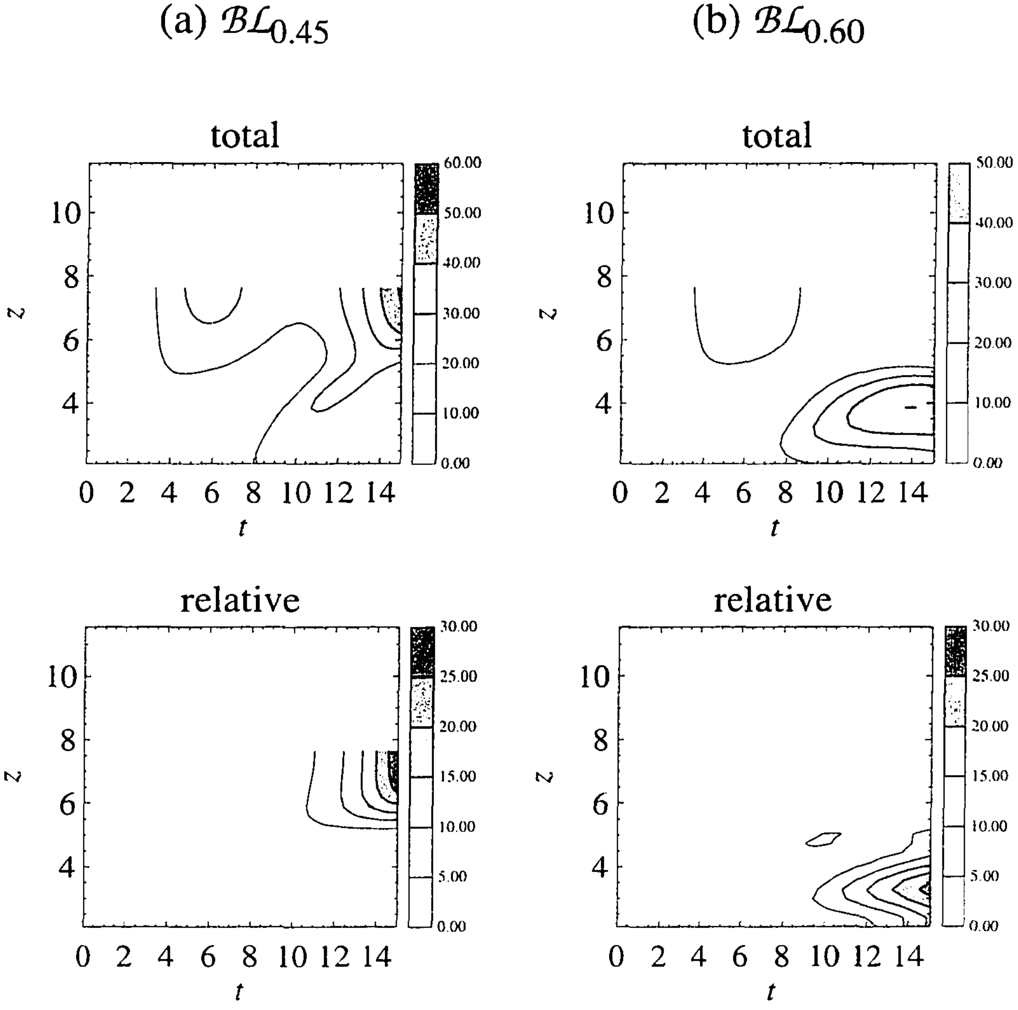

(a) $\mathcal{BL}_{0.45}$

(b) $\mathcal{BL}_{0.60}$

Figure 3.5: Total (top) and relative (bottom) wave activity density for the case of a low rigid upper boundary: (a) $\mathcal{BL}_{0.45}$ (η_o=0.45); (b) $\mathcal{BL}_{0.60}$ (η_o=0.60).

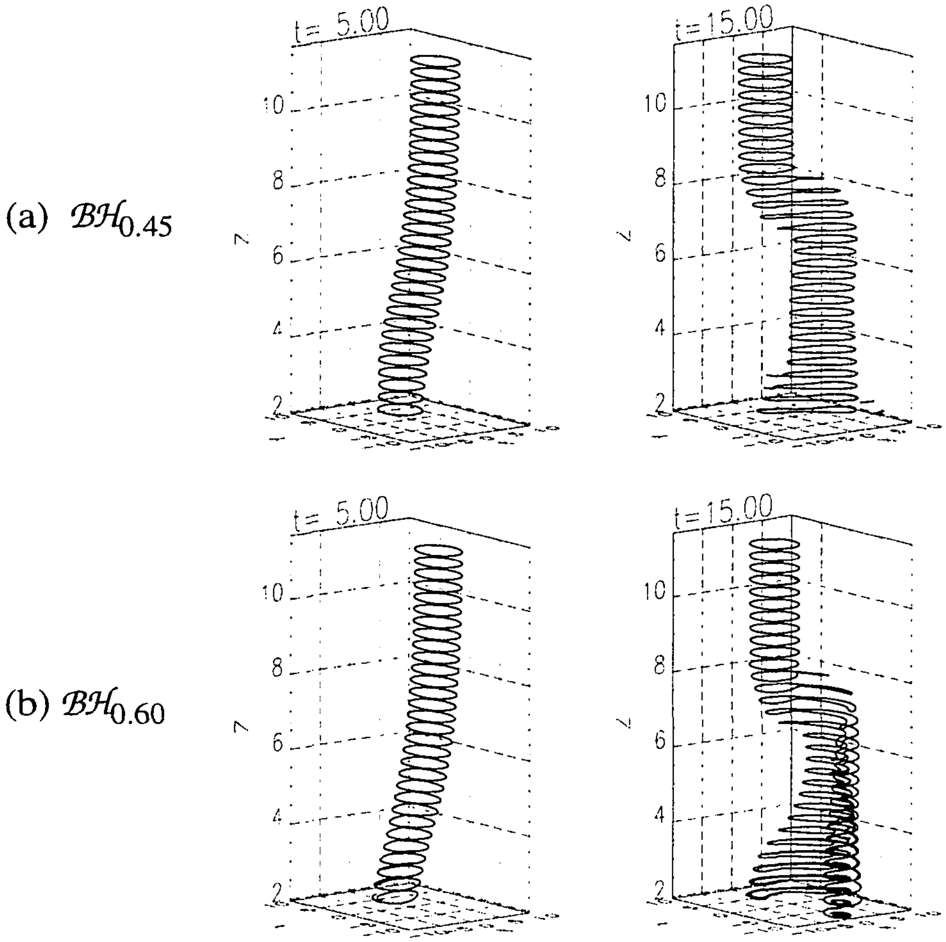

Figure 3.6: As in Figure 3.3 for the case of a high rigid upper boundary: (a) $\mathcal{BH}_{0.45}$ (η_o=0.45); (b) $\mathcal{BH}_{0.60}$ (η_o=0.60).

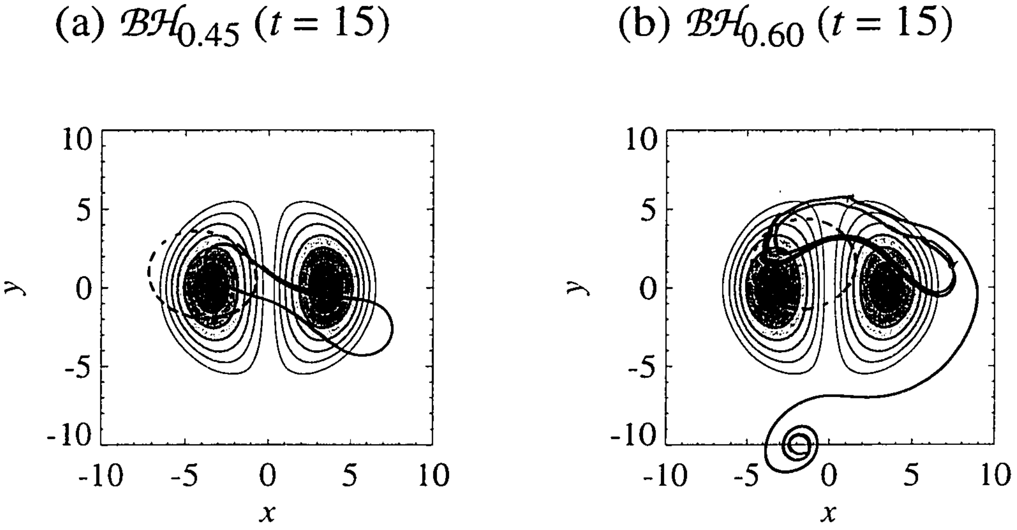

(a) $\mathcal{BH}_{0.45}$ ($t = 15$)

(b) $\mathcal{BH}_{0.60}$ ($t = 15$)

Figure 3.7: As in Figure 3.4 for the case of a high rigid upper boundary: (a) $\mathcal{BH}_{0.45}$ (η_o=0.45); (b) $\mathcal{BH}_{0.60}$ (η_o=0.60).

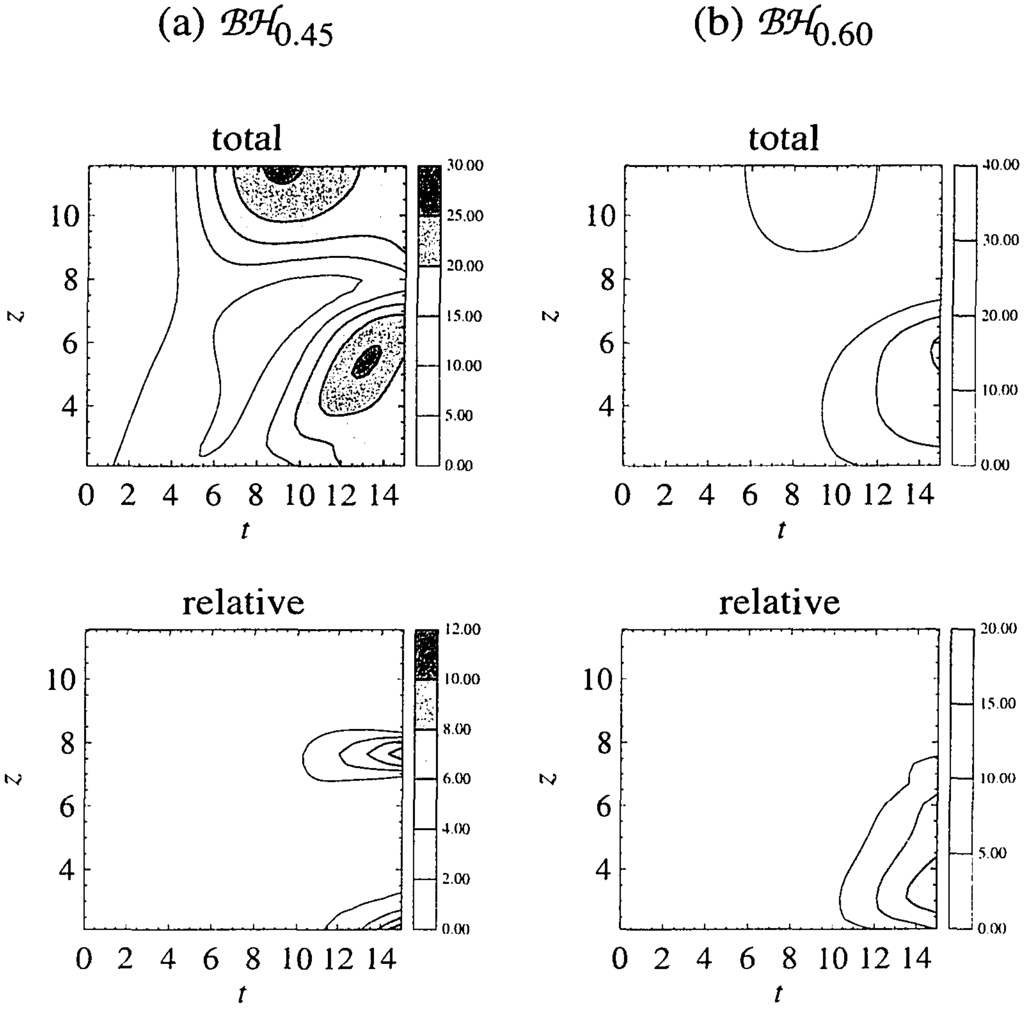

Figure 3.8: As in Figure 3.5 for the case of a high rigid upper boundary: (a) $\mathcal{BH}_{0.45}$ (η_o=0.45); (b) $\mathcal{BH}_{0.60}$ (η_o=0.60).

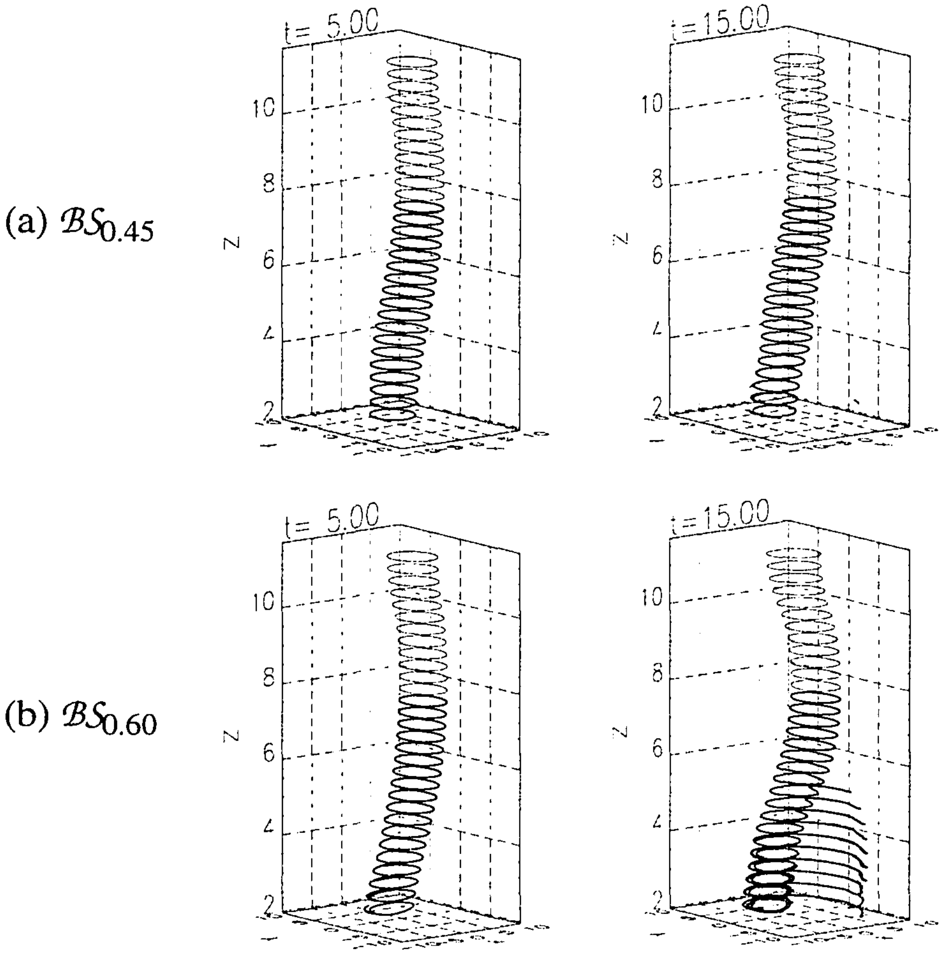

Figure 3.9: As in Figure 3.3 for the case of a vertical sponge (α_T=1.6): (a) $\mathcal{BS}_{0.45}$ (η_o=0.45); (b) $\mathcal{BS}_{0.60}$ (η_o=0.60). The thin solid contours lie within the vertical sponge.

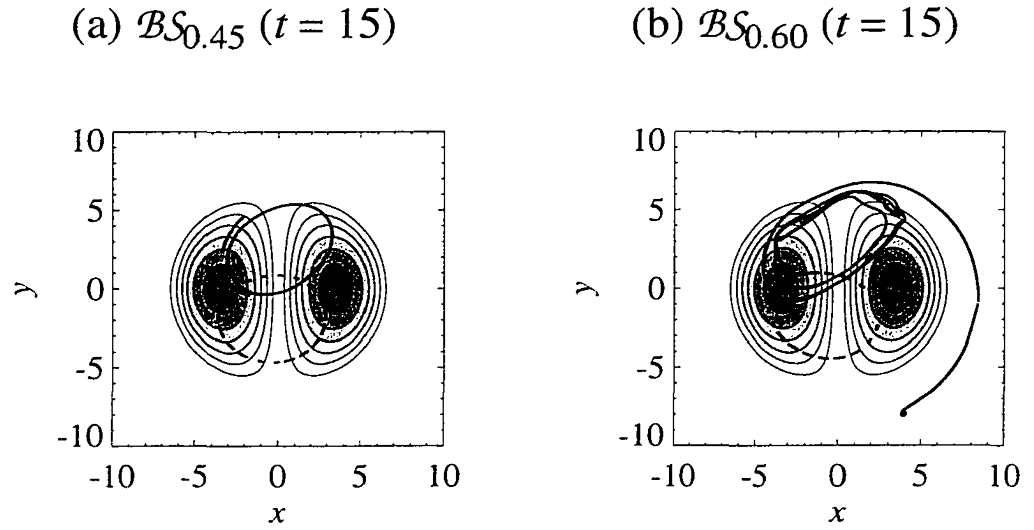

Figure 3.10: As in Figure 3.4 for the case of a vertical sponge (α_T=1.6): (a) $\mathcal{BS}_{\mathbf{0.45}}$ ($\eta_\circ$=0.45); (b) $\mathcal{BS}_{\mathbf{0.60}}$ ($\eta_\circ$=0.60).

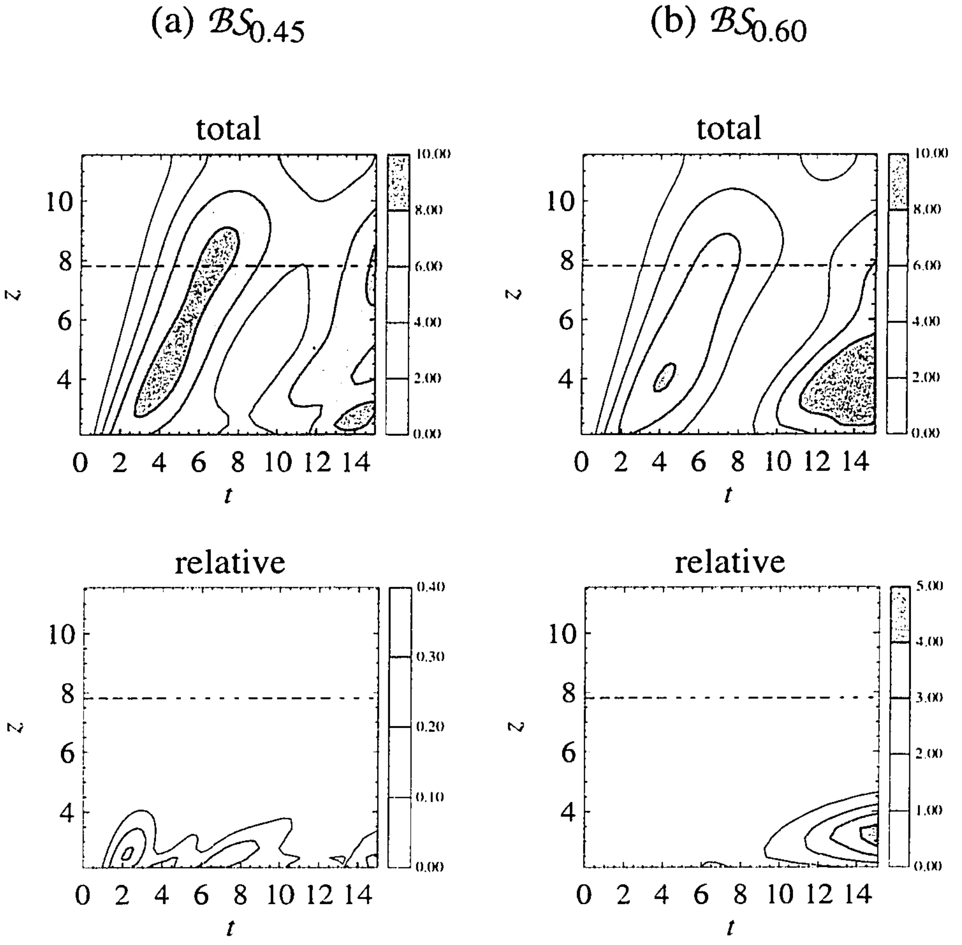

Figure 3.11: As in Figure 3.5 for the case of a vertical sponge (α_T=1.6): (a) $\mathcal{BS}_{0.45}$ (η_o=0.45); (b) $\mathcal{BS}_{0.60}$ (η_o=0.60). The vertical sponge bottom is indicated by the horizontal dashed line.

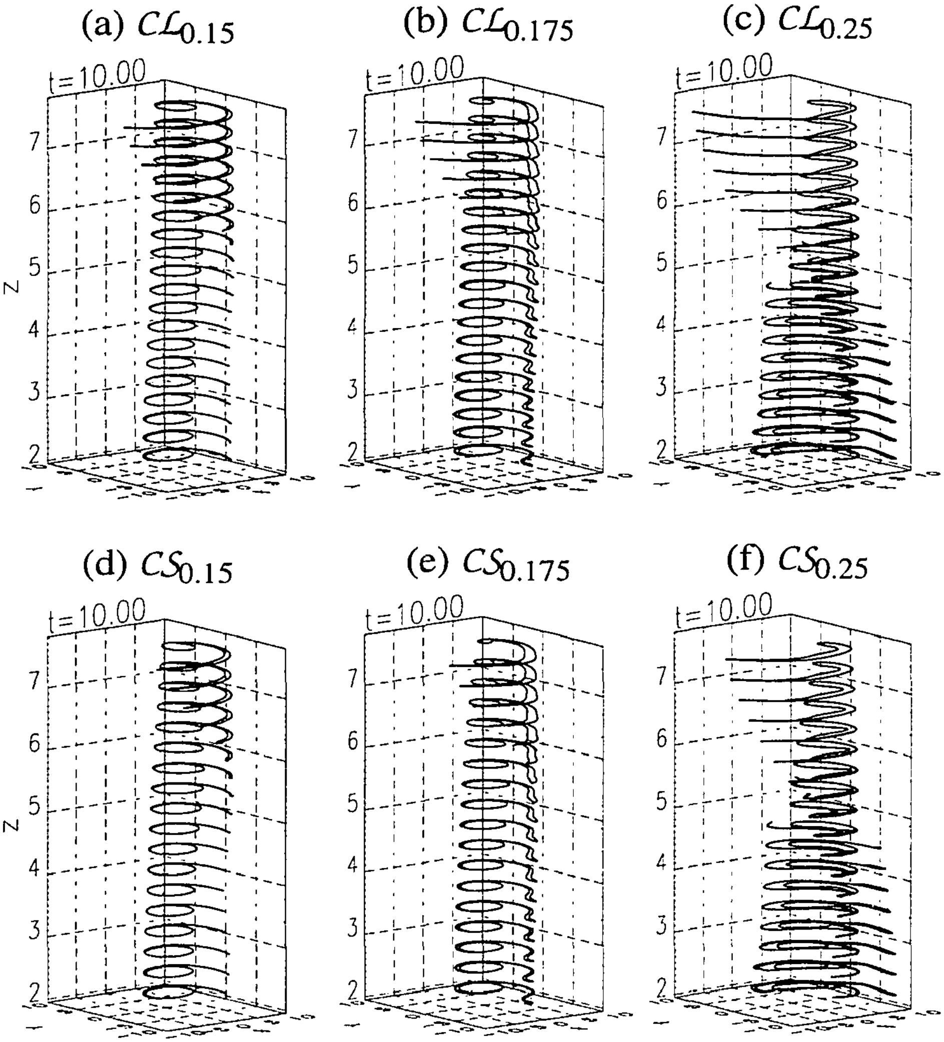

Figure 3.12: Perspective views of a compressible vortex. Low rigid upper boundary cases: (a) $\mathcal{CL}_{0.15}$ (η_o=0.15); (b) $\mathcal{CL}_{0.175}$ (η_o=0.175); (c) $\mathcal{CL}_{0.25}$ (η_o=0.25). Vertical sponge cases: (d) $\mathcal{CS}_{0.15}$ (η_o=0.15); (e) $\mathcal{CS}_{0.175}$ (η_o=0.175); (f) $\mathcal{CS}_{0.25}$ (η_o=0.25). Note that the plots do not include the region of the vertical sponge.

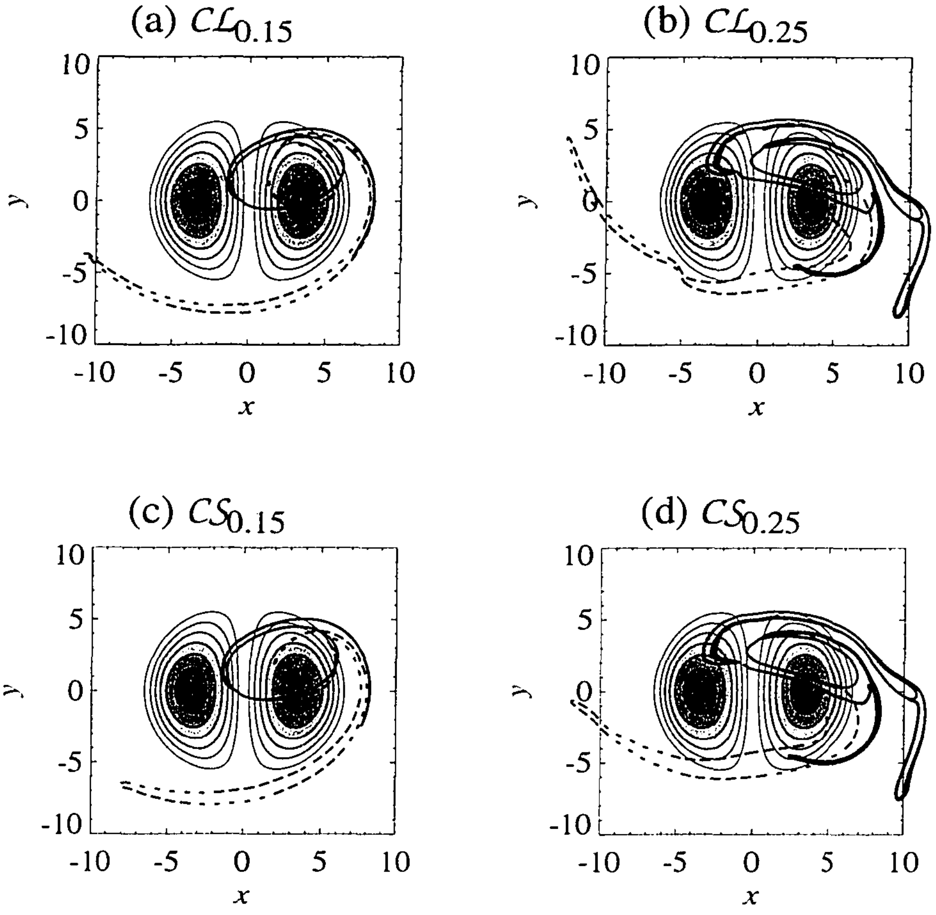

Figure 3.13: Upper-level (dotted) and bottom-level (solid) potential vorticity contours: Low rigid upper boundary cases: (a) $\mathcal{CL}_{0.15}$ (η_o=0.15); (b) $\mathcal{CL}_{0.25}$ (η_o=0.25). Vertical sponge cases: (c) $\mathcal{CS}_{0.15}$ (η_o=0.15); (d) $\mathcal{CS}_{0.25}$ (η_o=0.25).

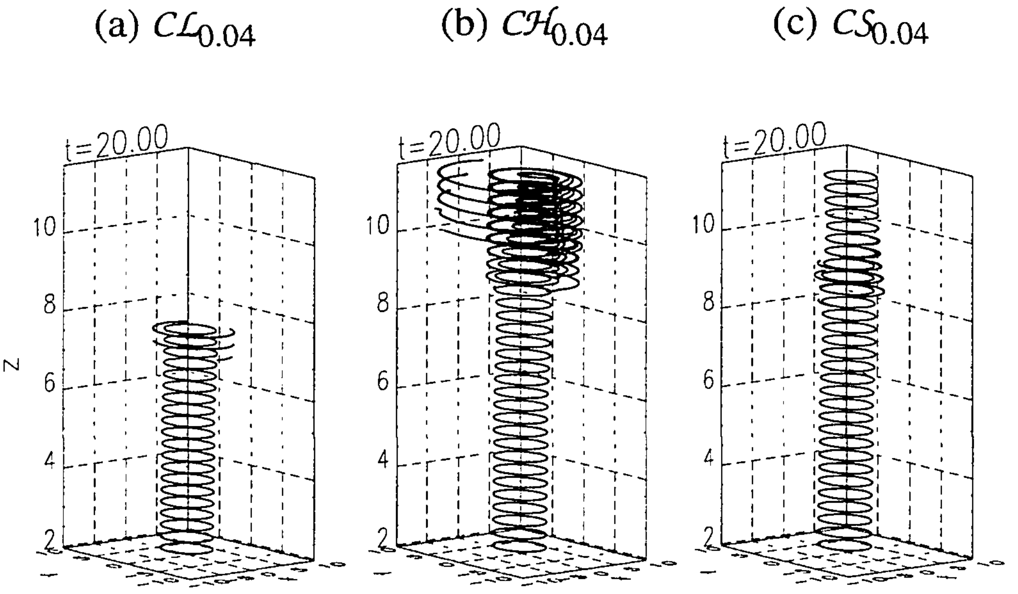

Figure 3.14: Perspective views of a compressible vortex for a very weak forcing amplitude of η_o=0.04. (a) Low rigid lid: $C\mathcal{L}_{\mathbf{0.04}}$; (b) High rigid lid: $C\mathcal{H}_{\mathbf{0.04}}$; (c) Vertical sponge: $C\mathcal{S}_{\mathbf{0.04}}$.

Chapter 4

A new mechanism for planetary wave breaking

In Chapter 3 we investigated the effects of upper boundaries on planetary wave breaking. Through the incorporation of an absorbing sponge layer in the CD/CS model we were able to limit back reflections from the top of the model and in so doing better represent wave breaking processes. In this Chapter, we investigate a possible mechanism for planetary wave breaking.

FH investigated the interaction of equatorward-propagating Rossby waves and zonal mean flows, where the latter were initially free of any critical lines (i.e., locations where the phase speed of the waves match the speed of zonal mean flow). If the initial zonal mean flow were to contain a critical line then critical layer theory (Warn and Warn, 1976, 1978; Killworth and McIntyre, 1985) demonstrates that wave breaking will occur in the vicinity of the critical level. However, the question addressed in FH was whether or not wave breaking can occur without critical lines in the zonal mean flow (as often appears to be the case in the real atmosphere).

The main result from FH is termed the "two-fifths" rule for Rossby wave breaking. In FH a stationary Rossby wave, sinusoidal in longitude was slowly switched on, and the meridional propagation of the resulting wave front through a shear flow was examined. It was shown that under slowly-varying conditions in an inviscid quasi-linear model (i.e., one without any wave-wave interactions), a steady state was obtained if, and only if, the zonal mean flow was decelerated by less than two-fifths of its initial value as a result of the passage of the wave front. If the passage caused a larger zonal mean flow reduction, a pile-up of wave activity density in the shear layer was seen to culminate in the generation of a critical layer. The physical explanation for this behaviour is as follows. The passing wave front causes a mean flow deceleration which acts to reduce the group velocity. In the shear layer, the deceleration and the reduction in group velocity are not uniform, being largest in regions with the smallest initial winds. This causes the wave activity to pile up in such regions. For a steady state to emerge, the wave activity must increase proportionately to the decrease in group velocity so that there will be no prolonged convergence of wave activity into the shear layer. However, the increase in wave activity again reduces the mean winds and the group velocity. If the two-fifths rule is violated, this process does not converge; instead the slowly varying theory predicts that the mean flow deceleration and the pile-up of wave activity will continue until a critical layer forms. FH noted that this qualitative picture was preserved in the quasi-linear model when the slowly-varying assumption was relaxed.

Figure 4.1 illustrates graphically the mathematical basis of FH's two-fifths rule for wave breaking. The curves represent the relationship between wave activity density A and zonal meal flow $\overline{u}$ in the steady state for different forcing amplitudes η. The straight line represents the relation between A and $\overline{u}$ that exists at all time for flows evolving from initial zonal mean flow $\overline{u}^{\circ}$. Intersections between the straight line and the curves represent possible steady states for the given η and $\overline{u}^{\circ}$. It is evident from Figure 4.1 that there exists a critical forcing denoted η^{c} (corresponding to the dashed curve) beyond which no steady states exist for the given $\overline{u}^{\circ}$. Corresponding to this critical forcing, there is a corresponding critical wave activity density A^{c} and zonal mean flow $\overline{u}^{c}$. FH showed that $A^{c} = 2\overline{u}^{\circ}/5$ and $\overline{u}^{c} = 3\overline{u}^{\circ}/5$, which are the basis of the two-fifths rule for wave breaking, i.e., wave breaking occurs if the zonal mean flow decelerates by more than $2\overline{u}^{\circ}/5$.

As stated, FH's investigation was focused on equatorward-propagating Rossby waves. In this investigation we attempt to generalize the rule to our vertically-propagating planetary wave situation. The numerical model we will use is the CD/CS model described in Chapter 2. This particular model, as opposed to the pseudo-spectral one used by FH, will allow us to describe wave breaking in much greater detail. In Section 4.1 we develop an analytical theory for the breakdown of vertically-propagating planetary waves. In Section 4.2 we numerically investigate the system when the assumptions of the analytical theory are relaxed. The results are summarized in Section 4.3. We note that most of the results of this Chapter have been submitted for publication (Wang and Fyfe, 1998).

Here we briefly introduce the model setup used in this Chapter. We initialize the system with a cylindrical PV column, or vortex, with radius $r_{\circ}$ centered on the North

Pole. The vortex edge separates interior and exterior regions of uniform PV, $Q_i(z)$ and $Q_o(z)$, respectively (the initial vortex edge is shown in plan view in Figure 4.2). Note that the PV jump across the vortex edge, $\Delta Q(z) \equiv Q_i(z) - Q_o(z)$, varies with height. By carefully setting $\Delta Q(z)$ we are able to introduce a zonal mean shear flow in the middle layers of the domain. Vertically the model is bounded by rigid surfaces at the bottom and top. The bottom surface describes a large spatial scale topography shown by the shaded contours in Figure 4.2. In the numerical simulations described in Section 4.2, the topography is switched on slowly (to a maximum at $t_s = 10$) in order to produce an upward-propagating wave *front* which interacts with the shear flow. Note that the slow switch-on, aside from generating a wave front, limits the generation of undesirable wave transients. To prevent back reflections of the upward-propagating waves, an absorbing sponge is placed underneath the rigid-lid.

4.1 Theory

In what follows we invoke the Boussinesq approximation and express the underlying equations in polar cylindrical coordinates. The plan is to first present the quasi-linear equations for the system and then derive a dispersion relationship for planetary waves whose vertical wavelengths are much smaller than any vertical variations in the background state (i.e., we invoke the WKB assumption). Following this we will derive wave activity density and zonal mean flow evolution equations, which together with the dispersion relation allow us to derive a rule for vertically-propagating planetary wave breaking.

4.1.1 Quasi-linearization

The linearized equation governing a small amplitude disturbance $\psi'(\lambda, r, z, t)$ to a zonally-averaged mean state $\overline{\psi}(r, z, t)$ is

$$\frac{\partial q'}{\partial t} + \frac{\overline{u}}{r}\frac{\partial q'}{\partial \lambda} + \frac{\partial \overline{q}}{\partial r}v' = 0 \text{ where} \tag{4.1}$$

$$\begin{aligned}
v'(\lambda, r, z, t) &= -\frac{1}{r}\frac{\partial \psi'}{\partial \lambda}, && (4.2)\\
q'(\lambda, r, z, t) &= \frac{1}{r}\frac{\partial}{\partial r}\left(r\frac{\partial \psi'}{\partial r}\right) + \frac{1}{r^2}\frac{\partial^2 \psi'}{\partial \lambda^2} + \frac{1}{B}\frac{\partial^2 \psi'}{\partial z^2}, && (4.3)\\
\overline{u}(r, z, t) &= \frac{\partial \overline{\psi}}{\partial r} \text{ and} && (4.4)\\
\overline{q}(r, z, t) &= \frac{1}{r}\frac{\partial}{\partial r}\left(r\frac{\partial \overline{\psi}}{\partial r}\right) + \frac{1}{B}\frac{\partial^2 \overline{\psi}}{\partial z^2}, && (4.5)
\end{aligned}$$

where λ, r and z are the zonal (or azimuthal), meridional (or radial) and vertical directions, respectively. The zonal average is written as $\overline{()} = 1/(2\pi)\int_0^{2\pi}()d\lambda$ and $B = g^2/(c_p T_{\circ\circ} f_\circ^2)$ (where g is gravity acceleration, c_p is specific heat capacity at constant pressure, $T_{\circ\circ}$ a constant reference temperature and $f_\circ{=}2\Omega$ is the constant Coriolis parameter with Ω being the angular rotation rate of Earth). The equation governing the zonally-averaged zonal flow (with the residual mean transport term, $f_\circ \overline{v_a^*}$, neglected as justified later in this Chapter) is

$$\frac{\partial \overline{u}}{\partial t} = \frac{1}{\rho_\circ r}\nabla \cdot \mathbf{S}$$

where $\mathbf{S} = \left[S^{(\lambda)}, S^{(r)}, S^{(z)}\right] = \left[0, -\rho_\circ r\overline{u'v'}, -(\rho_\circ r/B)\overline{v'\partial\psi'/\partial z}\right]$ (Andrews et al., 1987).

Note that the system is nondimensionalized as before with time scale $S{=}4\pi/f_\circ$, vertical length scale $H{=}RT_{\circ\circ}/g$ and horizontal length scale $L{=}N_\circ H/f_\circ$ (R being the ideal gas constant and $N_\circ$ the Brunt-Väisälä frequency). Eq. (4.1) is linear in ψ' but because of the fact that the time-varying mean state $\overline{\psi}(r, z, t)$ depends on second order disturbance quantities (as we shall see) it is referred to as a "quasi-linear" equation.

In order to make analytical progress with Eq. (4.1) we require that $\partial\overline{q}/\partial r$ be time-invariant. In FH this was true under their assumption that the mean state was slowly varying in the meridional direction. In this study the assumed piecewise-uniform distribution of PV does not allow us to assume slow variations in the meridional (i.e., radial) direction so we assume

$$\frac{\partial\overline{q}}{\partial r} = \left.\frac{\partial\overline{q}}{\partial r}\right|_{t=0} = -\Delta Q(z)\delta(r - r_{\circ})$$

where $\Delta Q(z) = Q_i(z) - Q_o(z)$ is the PV jump across the vortex edge and δ is the Dirac delta function. The validity of the assumption that $\partial\overline{q}/\partial r$ is time-invariant will be judged later when we compare our theoretical predictions (given this assumption) with our numerical simulations (without this assumption). We note that the subsequent theoretical development can be generalized to include the special case of a circular contour shifted a finite distance ϵ off the pole, in which case

$$\frac{\partial\overline{q}}{\partial r} = -\frac{\Delta Q(z)}{\pi\sqrt{\epsilon^2 - (r_{\circ} - r)^2}}h(r) \text{ where}$$

$$h(r) = \begin{cases} 0 & \text{if} \quad |r - r_{\circ}| > \epsilon, \\ 1 & \text{if} \quad |r - r_{\circ}| \leq \epsilon. \end{cases} \tag{4.6}$$

Finally, take note that all the calculations to follow have $r_{\circ} = 3$ and $B \approx 1.0$.

4.1.2 Dispersion relation and vertical group velocity

To solve Eq. (4.1) we assume a wave solution

$$\psi'(\lambda, r, z, t) = \tilde{\psi}(r, z)e^{i(s\lambda - \sigma t)} \quad \text{and} \quad q'(\lambda, r, z, t) = \tilde{q}(r, z)e^{i(s\lambda - \sigma t)} \tag{4.7}$$

where s is the zonal wave number and σ the frequency (both constant and real). Substituting the above into Eq. (4.1) produces $\tilde{q} = s\overline{q}_r\tilde{\psi}/(\overline{u}s - \sigma r)$ which upon further substitution into Eq. (4.3) yields

$$\frac{1}{r}\frac{\partial}{\partial r}\left(r\frac{\partial\tilde{\psi}}{\partial r}\right) + \frac{1}{B}\frac{\partial^2\tilde{\psi}}{\partial z^2} = \left(\frac{s\overline{q}_r}{\overline{u}s - \sigma r} + \frac{s^2}{r^2}\right)\tilde{\psi} \equiv V(r, z)\tilde{\psi}. \tag{4.8}$$

Note that this equation is time-independent except parametrically through the dependence of V on $\overline{u}(r, z, t)$. We now invoke WKB theory under the assumption that V is a slowly-varying function of z, i.e., $V = V(r, Z)$, where $Z = \nu z$ and ν is a small dimensionless parameter (in what follows we take $\nu = 0.1$). Thus, Z is a "stretched" variable compared to z. We now seek local wave solutions,

$$\tilde{\psi} = \Theta(r, Z)\Lambda(z, Z) \tag{4.9}$$

where Θ is real and Λ is complex, and which after substitution into Eq. (4.8) yields

$$\frac{1}{\Theta}\left[\frac{1}{r}\frac{\partial}{\partial r}\left(r\frac{\partial\Theta}{\partial r}\right) - V(r, Z)\Theta\right] = -\frac{1}{\Lambda}\left[\frac{1}{B}\frac{\partial^2\Lambda}{\partial z^2}\right]. \tag{4.10}$$

Since the left-hand-side is only a function of r and Z and the right-hand-side only a function of z and Z it must be the case that both sides are equal to a function of the stretched variable Z alone, call it $C(Z)$. We thus obtain the following equations:

$$\frac{1}{r}\frac{\partial}{\partial r}\left(r\frac{\partial\Theta}{\partial r}\right) - V(r, Z)\Theta - C(Z)\Theta = 0, \tag{4.11}$$

$$\frac{\partial^2\Lambda}{\partial z^2} + BC(Z)\Lambda = 0. \tag{4.12}$$

Solution to Eq. (4.11)

(a) $r \neq r_\circ$

Eq. (4.11) is singular at $r_\circ$ because of the δ-function behaviour of $\overline{q}_r$ [recall the definition of V in Eq. (4.8)]. Away from $r_\circ$ where $\overline{q}_r$ is zero Eq. (4.11) is a modified Bessel equation whose general solution is

$$\Theta(r,Z) = C_1 I_s(\sqrt{C}r) + C_2 K_s(\sqrt{C}r), \tag{4.13}$$

where C_1 and C_2 are, at this point, unknown functions of Z (I_s and K_s are modified Bessel functions of the first and second kind, respectively). Note that $I_s(\sqrt{C}r) \to \infty$ as $r \to \infty$ and $K_s(\sqrt{C}r) \to \infty$ as $r \to 0$. Demanding that Θ be bounded as $r \to \infty$ and $r \to 0$ produces two solution branches for Θ, i.e., one where $C_1 = 0$ for $r > r_\circ$ and another where $C_2 = 0$ for $r < r_\circ$. Matching the two branches of Θ as $r \to r_\circ$ yields $C_1 = B_s K_s(\sqrt{C}r_\circ)$ and $C_2 = B_s I_s(\sqrt{C}r_\circ)$. Thus we have

$$\Theta(r,Z) = \begin{cases} B_s K_s(\sqrt{C}r_\circ) I_s(\sqrt{C}r) & r < r_\circ, \\ B_s I_s(\sqrt{C}r_\circ) K_s(\sqrt{C}r) & r > r_\circ, \end{cases} \tag{4.14}$$

where B_s is obtained from the following normalization constraint (following the usual standard procedure), $\int_0^\infty r\Theta^2\, dr = 1$, i.e.,

$$B_s^2 = \frac{8}{r_\circ^2[I_s^2(\sqrt{C}r_\circ)X^2 - K_s^2(\sqrt{C}r_\circ)Y^2]} \quad \text{where} \tag{4.15}$$

$$X = K_{s-1}(\sqrt{C}r_\circ) + K_{s+1}(\sqrt{C}r_\circ) \;\; \text{and} \;\; Y = I_{s-1}(\sqrt{C}r_\circ) + I_{s+1}(\sqrt{C}r_\circ).$$

(b) $r = r_\circ$

We now return to the general equation (4.11) which is valid for all r, including $r_\circ$. As noted, Eq. (4.11) is singular at $r_\circ$ because of the δ-function behaviour of $\bar{q}_r$. To find the so-called "jump condition" which ensures that Θ in Eq. (4.14) solves Eq. (4.11) at $r_\circ$ we apply the operator $\lim_{\epsilon\to 0}\int_{r_\circ-\epsilon}^{r_\circ+\epsilon} r()\ dr$ to Eq. (4.11) (Yih, 1980). Here ϵ is a small and real number. This yields (after some manipulation):

$$\lim_{\epsilon\to 0}\left[r\frac{\partial\Theta}{\partial r}\right]_{r_\circ-\epsilon}^{r_\circ+\epsilon} = -\frac{sr_\circ\Delta Q}{\bar{u}_\circ s-\sigma r_\circ}\Theta_\circ, \tag{4.16}$$

where $\bar{u}_\circ = \bar{u}(r_\circ, Z, t)$ and $\Theta_\circ = \Theta(r_\circ, Z)$. Using Θ from Eq. (4.14) in the above yields the following constraint on the frequency of the waves:

$$\sigma = s\left[\frac{\bar{u}_\circ}{r_\circ} - \Delta Q K_s\left(\sqrt{C}r_\circ\right) I_s\left(\sqrt{C}r_\circ\right)\right]. \tag{4.17}$$

Solution to Eq. (4.12)

Since by assumption the coefficient $C(Z)$ in Eq. (4.12) is slowly-varying we can use standard WKB theory (Nayfeh, 1981) to obtain

$$\Lambda(z,Z) = \frac{\Lambda_\circ}{\sqrt{m(Z)}}e^{i\int m(Z)dz} \tag{4.18}$$

where $\Lambda_\circ$ is a constant (determined from the lower boundary condition) and $m(Z)$ is the vertical wave number satisfying $m = \sqrt{BC}$. The dispersion relationship for the system follows from Eq. (4.17), i.e.,

$$\sigma = s\left[\frac{\bar{u}_\circ}{r_\circ} - \Delta Q K_s\left(\frac{m}{\sqrt{B}}r_\circ\right) I_s\left(\frac{m}{\sqrt{B}}r_\circ\right)\right]. \tag{4.19}$$

Solutions to this equation exist only when $0 < \bar{u}_\circ/(r_\circ\Delta Q) - \sigma/(s\Delta Q) < (2s)^{-1}$. Finally, the vertical group velocity, C_g, is given by

$$C_g \equiv \frac{\partial\sigma}{\partial m}$$

$$= \frac{s\Delta Q r_\circ}{2\sqrt{B}}\left\{I_s\left(\frac{m}{\sqrt{B}}r_\circ\right)\left[K_{s-1}\left(\frac{m}{\sqrt{B}}r_\circ\right)+K_{s+1}\left(\frac{m}{\sqrt{B}}r_\circ\right)\right]\right.$$
$$\left. -K_s\left(\frac{m}{\sqrt{B}}r_\circ\right)\left[I_{s-1}\left(\frac{m}{\sqrt{B}}r_\circ\right)+I_{s+1}\left(\frac{m}{\sqrt{B}}r_\circ\right)\right]\right\}. \qquad (4.20)$$

We will use both Eqs. (4.19) and (4.20), as well as their approximate forms which we now derive.

Asymptotic forms

For large $x = mr_\circ/\sqrt{B}$ (i.e., small vertical wavelength, which is our WKB limit) we have the asymptotic formulae for the modified Bessel functions $I_s(x)$ and $K_s(x)$ (see Watson, 1944):

$$I_s(x) \approx \sqrt{\frac{e^{2x}}{2\pi x}}\left[1+\frac{1-4s^2}{1!8x}+\frac{(1-4s^2)(9-4s^2)}{2!(8x)^2}+\cdots\right],$$
$$K_s(x) \approx \sqrt{\frac{2}{\pi x e^{2x}}}\left[1-\frac{1-4s^2}{1!8x}+\frac{(1-4s^2)(9-4s^2)}{2!(8x)^2}+\cdots\right].$$

Retaining only the first term in each of these expressions leads to

$$\sigma \approx s\left[\frac{\overline{u}_\circ}{r_\circ}-\frac{\Delta Q}{\pi}\left(\frac{m}{\sqrt{B}}r_\circ\right)^{-1}\right] \quad \text{and} \qquad (4.21)$$

$$C_g \approx \frac{s\Delta Q r_\circ}{\pi\sqrt{B}}\left(\frac{m}{\sqrt{B}}r_\circ\right)^{-2} \approx \frac{s r_\circ \pi}{\Delta Q\sqrt{B}}\left(\frac{\overline{u}_\circ}{r_\circ}-\frac{\sigma}{s}\right)^2 \qquad (4.22)$$

As can be seen the vertical group velocity (in this limit) is proportional to the square of the zonal mean flow at $r_\circ$. This contrasts to the meridionally-propagating case treated in FH where the horizontal group velocity is more weakly dependent on the zonal mean flow (specifically, it is proportional to the zonal mean flow to the power 1.5).

Illustration

Here we illustrate our results gained so far. Consider a vortex initially centered on the pole with radius $r_o = 3$ and PV jump ΔQ which varies with Z as shown in Figure 4.3(a). We use Z^* to represent the centre of the shear region. For this PV distribution the solid curve in Figure 4.3(b) shows the zonal mean flow at r_o. For a stationary ($\sigma = 0$) planetary wave with gravest zonal wavenumber ($s = 1$) we plot in Figures 4.3(c) and (d) (solid curves) the vertical wavelength $L_W = 2\pi/m$ and group velocity C_g. L_W and C_g are calculated using the exact expressions in Eqs. (4.19) and (4.20). As can be seen the vertical wavelength and group velocity are smallest in the shear region at $Z^* \approx 10$. We note also that the vertical wavelengths are, by design, small compared to the width of the shear region (i.e., the zonal mean flow is slowly varying).

The dashed curve in Figure 4.3(b) was obtained from a simulation with the CD/CS numerical model (described in Chapter 2) initialized with the zonal mean flow given by the solid curve. The system was forced from below with a slowly switched-on $s = 1$ topography (as shown in Figure 4.2) with $\eta_o = 0.12$. Note that an absorbing sponge exists above $Z = 20$ in order to limit back reflections. At this time in the simulation (i.e., $t = 100$) the system has reached equilibrium and the passage of the wave front has caused the zonal mean flow to be decreased everywhere. Shown in Figures 4.3(c) and (d) (dashed curves) are the corresponding L_W and C_g profiles computed diagnostically using Eqs. (4.19) and (4.20), respectively. As can be seen, the decelerated zonal mean flow implies smaller vertical wavelengths and slower group velocities.

4.1.3 Wave activity evolution equation

The wave activity density A for this quasi-linear model is given by

$$A(z,t) = 2\pi\rho_o r_o^2 \Delta Q \overline{\eta'^2}|_{r_o}. \tag{4.23}$$

where $\overline{\eta'^2}|_{r_o}$ is the mean square particle displacement in the radial direction from $r = r_o$ (see Appendix A). This expression is valid for small displacements from $r = r_o$. In two steps we now derive the wave activity evolution equation

$$\frac{\partial A}{\partial t} + \frac{\partial}{\partial z}(C_g A) = 0. \tag{4.24}$$

Step 1

Multiplying the well-known particle displacement equation $\partial\eta'/\partial t + (\overline{u}/r)\partial\eta'/\partial\lambda = v'$ (Andrews et al., 1987) by $4\pi\rho_o r_o^2 \eta' \Delta Q$ zonally averaging along r_o and using the definition of wave activity density yields

$$\frac{\partial A}{\partial t} - 4\pi\rho_o r_o^2 \Delta Q \overline{\eta' v'}|_{r_o} = 0. \tag{4.25}$$

Applying the operator $\int_0^\infty r dr$ to the Eliassen-Palm flux equation $\nabla \cdot \mathbf{S} = -\rho_o r \overline{v' q'}$ yields

$$\frac{\partial S}{\partial z} + 4\pi\rho_o r_o^2 \Delta Q \overline{\eta' v'}|_{r_o} = 0, \tag{4.26}$$

where $S \equiv 4\pi \int_0^\infty r S^{(z)} dr$. Note that to obtain this equation we have used the facts that for plane waves, $\overline{u'v'} = 0$ and $\int_0^\infty r^2 \overline{v' q'} dr = r_o^2 \Delta Q \overline{v' \eta'}|_{r_o}$ (see Appendix B). Finally, adding Eqs. (4.25) and (4.26) gives

$$\frac{\partial A}{\partial t} + \frac{\partial S}{\partial z} = 0. \tag{4.27}$$

Step 2

We now relate A and S. Substituting $\eta' = \tilde{\eta} e^{i(s\lambda - \sigma t)}$ and $v' = -is\psi'/r$ into the particle displacement equation gives $\eta' = s\psi'/(\sigma r - \overline{u}s)$ or $\overline{\eta'^2} = 0.5 s^2 \overline{\psi'^2}|_{r_\circ}/(\sigma r_\circ - \overline{u}_\circ s)^2$. This result, along with the facts from the previous subsection that $\overline{\psi'^2} = 0.5\Theta^2|\Lambda|^2 = 0.5 B_s^2 K_s^2(\sqrt{C}r_\circ) I_s^2(\sqrt{C}r_\circ)|\Lambda|^2$ and $\sigma r_\circ - \overline{u}_\circ s = -s r_\circ \Delta Q K_s(\sqrt{C}r_\circ) I_s(\sqrt{C}r_\circ)$, allows us to rewrite A in Eq. (4.23) as

$$A = \frac{\pi \rho_\circ B_s^2 |\Lambda|^2}{\Delta Q}.$$

As for S, we note that $v' = -is\psi'/r$, $\partial\psi'/\partial z = im\psi'$ and $\overline{\psi'^2} = 0.5\Theta^2|\Lambda|^2$ yield

$$S = \frac{2\pi \rho_\circ s m}{B} |\Lambda|^2,$$

where the previous normalization constraint $\int_0^\infty r\Theta^2 \, dr = 1$ has been used. With these expressions for A and S and replacing B_s^2 by (4.15), it follows that

$$\begin{aligned} S &= \frac{2sm\Delta Q}{BB_s^2} A \\ &= \frac{r_\circ^2 \Delta Q s m}{4B} \left\{ I_s^2\left(\frac{m}{\sqrt{B}} r_\circ\right) \left[K_{s-1}\left(\frac{m}{\sqrt{B}} r_\circ\right) + K_{s+1}\left(\frac{m}{\sqrt{B}} r_\circ\right) \right]^2 \right. \\ &\quad \left. - K_s^2\left(\frac{m}{\sqrt{B}} r_\circ\right) \left[I_{s-1}\left(\frac{m}{\sqrt{B}} r_\circ\right) + I_{s+1}\left(\frac{m}{\sqrt{B}} r_\circ\right) \right]^2 \right\} A. \end{aligned}$$

Further algebraic manipulation using the recurrence formula $I_s(x)K_{s+1}(x) + I_{s+1}(x)K_s(x) = 1/x$ and the group velocity expression in Eq. (4.20) yields,

$$S = C_g A.$$

This result together with Eq. (4.27), leads to the desired Eq. (4.24).

4.1.4 Zonal mean flow equation

Here we derive the following approximate relationship between the wave activity density at time t and the zonal mean flow change at $r_{\circ}$ between time $t = 0$ and t (denoted by $\Delta\overline{u}_{\circ}$)

$$A(z,t) = 4\pi\rho_{\circ}r_{\circ}^{2}\mathcal{E}(\Delta\overline{u}_{\circ})^{2}. \tag{4.28}$$

In this expression $\mathcal{E}$ is a prescribed function of ΔQ. We begin with the Transformed Eulerian Mean equation $\partial\overline{u}/\partial t = (\rho_{\circ}r)^{-1}\nabla\cdot\mathbf{S}$ where the residual mean transport term which ordinarily appears (i.e., $f_{\circ}\overline{v_{a}^{*}}$) can be neglected on the scale of the stretched vertical coordinate Z. Again using $\overline{v'q'} = -(\rho_{\circ}r)^{-1}\nabla\cdot\mathbf{S}$ and applying $\int_{0}^{\infty} dr$ yields

$$\frac{\partial}{\partial t}\int_{0}^{\infty}\overline{u}dr = -\int_{0}^{\infty}\overline{v'q'}dr = -\Delta Q\overline{v'\eta'}|_{r_{\circ}}, \tag{4.29}$$

where the right-hand-side is shown to follow in Appendix B. This relation together with Eqs. (4.26) and (4.27) and time-integration produces

$$A(z,t) = -4\pi\rho_{\circ}r_{\circ}^{2}\int_{0}^{\infty}\Delta\overline{u}dr \tag{4.30}$$

assuming that $A(z,0) = 0$. Finally, in Appendix C we approximately relate the radially-integrated zonal mean flow change to the zonal mean flow change at $r_{\circ}$ as:

$$\int_{0}^{\infty}\Delta\overline{u}dr = -\mathcal{E}(\Delta\overline{u}_{\circ})^{2}. \tag{4.31}$$

This with Eq. (4.30) yields Eq. (4.28).

4.1.5 The one-half rule for planetary wave breaking

We now derive a rule for planetary wave breaking following the approach set out in FH. Here we work with two equations, one connecting wave activity density and zonal mean flow in the steady state and another connecting wave activity density and zonal mean flow for all time. Equating $\partial A/\partial\overline{u}$ evaluated from both these equations establishes the critical steady state zonal mean flow.

From Eq. (4.24) with $\partial A/\partial t = 0$ we get $A = \beta C_g^{-1}$ where β is a constant. Given that $C_g = C_g\left(mr_\circ/\sqrt{B}\right)$ [Eq. (4.20)] and $\overline{u}_\circ = \overline{u}_\circ\left(mr_\circ/\sqrt{B}\right)$ [Eq. (4.19) with $\sigma = 0$], it is shown in Appendix D that

$$\frac{\partial A}{\partial \overline{u}_\circ} = \frac{2A}{r_\circ \Delta Q\, \mathcal{D}\left(\frac{m}{\sqrt{B}}r_\circ\right)}, \tag{4.32}$$

where $\mathcal{D}$ involves a complicated combination of modified Bessel functions. Take note that this expression is valid only for stationary steady state waves. At the same time we have the following expression which is valid for stationary waves at all time [recalling Eq. (4.28)]

$$\frac{\partial A}{\partial \overline{u}_\circ} = \frac{2A}{\overline{u}_\circ - \overline{u}_\circ^\circ} \tag{4.33}$$

where $\overline{u}_\circ^\circ$ denotes the value of $\overline{u}_\circ$ at $t = 0$. Equating (4.32) and (4.33) and using Eq. (4.28) produces the following equation involving the critical steady state values $\overline{u}_\circ^c$ and m^c, i.e.,

$$\frac{\overline{u}_\circ^c}{r_\circ \Delta Q} - \mathcal{D}\left(\frac{m^c}{\sqrt{B}}r_\circ\right) = \frac{\overline{u}_\circ^\circ}{r_\circ \Delta Q}. \tag{4.34}$$

At the same time from Eq. (4.19) with $\sigma = 0$, we have

$$\frac{\overline{u}_\circ^c}{r_\circ \Delta Q} - K_s\left(\frac{m^c}{\sqrt{B}}r_\circ\right) I_s\left(\frac{m^c}{\sqrt{B}}r_\circ\right) = 0. \tag{4.35}$$

With Eqs. (4.34) and (4.35) we have two equations in the two unknowns $\overline{u}_\text{o}^c/(r_\text{o}\triangle Q)$ and $m^c r_\text{o}/\sqrt{B}$. [Note that the empirically-derived function $\mathcal{E}(\triangle Q)$ now has been eliminated by the analysis.] Before deriving the exact solution to these equations, we note that for large $x = mr_\text{o}/\sqrt{B}$ it follows from Eq. (4.22) (with $\sigma = 0$) that $C_g \approx (s\pi/\triangle Q\sqrt{B}r_\text{o})\overline{u}_\text{o}^2$. Therefore given that $A = \beta C_g^{-1}$ we have that $\partial A/\partial\overline{u}_\text{o} \approx -2A/\overline{u}_\text{o}$, which together with (4.33) yields

$$\frac{\overline{u}_\text{o}^c}{\overline{u}_\text{o}^\text{o}} \approx \frac{1}{2}. \tag{4.36}$$

In other words, in this asymptotic limit, a steady state is possible if, and only if, the zonal mean flow at r_o is decelerated by less than one-half of its initial value. This contrasts with the smaller critical value of two-fifths derived by FH for the case of meridionally-propagating Rossby waves.

In Figure 4.4 we plot the exact (solid curve) and asymptotic (dashed line) critical ratio $\overline{u}_\text{o}^c/\overline{u}_\text{o}^\text{o}$ for a range of $\overline{u}_\text{o}^\text{o}/(r_\text{o}\triangle Q)$. Take note that from a previous comment no propagating wave solutions exist for $\overline{u}_\text{o}/(r_\text{o}\triangle Q) \geq 0.5$ (given $s = 1$ and $\sigma = 0$). As can be seen the exact critical ratio varies weakly with $\overline{u}_\text{o}^\text{o}/(r_\text{o}\triangle Q)$ and approximately converges to one-half as $\overline{u}_\text{o}^\text{o}/(r_\text{o}\triangle Q) \to 0$. This differs from FH in the sense that their critical ratio is independent of the initial zonal mean flow.

To summarize this section: we have formulated a quasi-linear, slowly-varying theory for the interaction between vertically-propagating planetary waves and vertically-sheared zonal mean flows. The theory predicts that planetary waves propagating through an initially westerly zonal mean flow will achieve a steady state only if the zonal mean flow at the vortex edge is decelerated by less than roughly one-half its initial value. To test this theory beyond its simplifying assumptions we now use our fully-nonlinear CD/CS numerical model.

4.2 Nonlinear numerical simulations

Before discussing our numerical results, we briefly review some of the features of the initial zonal mean wind used. As mentioned earlier, the PV jump across the vortex edge varies with height as shown in Figure 4.3(a). This determines an initial zonal mean wind with an hourglass distribution as shown in Figure 4.5. This zonal mean wind distribution is meant to resemble the winter stratospheric winds as indicated in Figure 4.6. Returning to Figure 4.5, the position of the minimum wind at each r is indicated by the horizontal dashed line at height Z^*. The position of the maximum wind at each Z is indicated by the vertical dashed line at radius r_o. The bold contour defines the zero wind line, which since it is so far away from the vortex edge does not play a direct role in the simulations to be described.

In the numerical experiments to be discussed we have used 120 vertical levels yielding about 10 levels per vertical wavelength and a domain which accommodates about 12 vertical wavelengths in total (with a sponge thickness of about 3 vertical wavelengths). The results which follow are insensitive to increased vertical levels and/or domain height. In this Chapter, we purposely switch on the topography slowly (i.e., the topography reaches its maximum at $t = 10$) to generate a wave front with $\sigma = 0$ which propagates toward the shear layer.

4.2.1 Verification of the one-half rule

A series of numerical experiments over a range of topographic amplitudes have been carried out and are summarized in Figure 4.7. In this figure the ratio, $\overline{u}_o/\overline{u}_o^o$ at Z^* (i.e., in the middle of the shear region), is plotted as a function of time (up to $t = 200$) for several topographic amplitudes (as labelled). For $\eta_o \leq 0.15$ this ratio remains unchanged when we continue the integrations up to $t = 300$. Inspecting these curves in this figure, we conclude that steady states are obtained only if $\eta_o \leq 0.15$ or equivalently, only if $\overline{u}_o/\overline{u}_o^o \leq 0.47$. The horizontal dashed line indicates that the theoretically predicted critical ratio obtained in the last subsection. One can see that the theoretical prediction is quite accurate in this case. For $\eta_o > 0.15$ the zonal mean wind decelerates beyond the theoretically predicted critical ratio and continues to slowly decelerate.

As indicated in Figure 4.7, and as characterized further in the following discussion, there appear to be three phases in the evolution of the system when $\eta_o > 0.15$: (I) an initial phase of deceleration as the wave front passes the shear layer (as in the steady cases); (II) an intermediate phase of small deceleration presumably involving enhanced zonal-mean-flow/group-velocity feedback and (III) a final rapid phase of wave breaking involving the migration of a stagnation point (i.e., a hyperbolic point of no-flow) across the vortex edge. To characterize the system further we now detail one of the steady and one of the unsteady (i.e., breaking) cases.

4.2.2 Steady case

Consider the $\eta_\circ = 0.12$ case shown in Figure 4.7. For this case we plot in Figure 4.8 contours of partical displacement from $r_\circ$, i.e., $\eta'|_{r_\circ}$. One can see very clearly upward wave propagation with the waves increasing in amplitude and decreasing in vertical wavelength in the shear layer. By $t = 100$ the waves have propagated into the sponge layer and the system has reached its steady state. Another perspective on the wave evolution is afforded by Figure 4.9 which shows the wave activity density as a function of height and time. Note that the wave activity density plotted here is defined by (A.1) and is normalized by $\eta_\circ^2$. As expected from our group velocity analysis the wave front slows as it approaches the shear layer (as indicated by the flattening of the isolines around Z^*). With regards to the zonal mean flow, Figure 4.10 shows that as the wave front propagates upward it leaves a trail of decelerated zonal mean flow behind (shaded). As predicted in Appendix C the largest deceleration occurs at the initial vortex edge (i.e., at $r = r_\circ = 3$) and in the middle of the shear layer (i.e., at Z^*) where the vortex displacement from its initial position is the greatest.

4.2.3 Unsteady case

Now consider the $\eta_\circ = 0.16$ case shown in Figure 4.7. For this stronger forcing the zonal mean wind at Z^* decelerates beyond the critical value and as such the system can not achieve a steady state. A perspective view of the vortex at $t = 166$ is shown in Figure 4.11. Within the shear layer at this time the vortex has clearly broken down. Figure 4.12 shows the events leading to the wave breaking (at Z^*). Following local overturning of the PV contour [Figure 4.12(a)] a thin filament stretches outside and wraps around the vortex [Figure 4.12(b)]. Very rapidly after the filament thins out to a point that it becomes separated from the main vortex [Figure 4.12(c)]. The filament then orbits the vortex until it is eventually surgically removed [Figure 4.12(d)]. A similar cycle of overturning, thinning, separation and expulsion follows at intervals of approximately 14 days. A similar process was observed by Polvani and Plumb (1992) for a two-dimensional perturbed vortex.

It has been observed that the initial overturning involves the migration of a stagnation point across the contour. This is shown in Figure 4.13(a) and (b), where the solid dot indicates the stagnation point and velocity vectors are indicated with arrows. Following the initial passage of the wave front and before t =150 (not shown) the PV contour slowly shifts towards the lower-left quadrant of the domain without significant departure from its initial circular shape (with the stagnation point being located well outside the contour). After $t \approx 150$, a region of high-curvature builds on the contour [Figure 4.13(a)] and when it becomes sufficiently high the contour overturns (i.e., the wave breaks). At precisely this time the stagnation moves inside the contour [Figure 4.13(b)]. The strain field around the stagnation point is shown in Figure 4.13(c) and (d). As can be seen, once the stagnation point crosses the contour, part of the contour is drawn towards an area of large negative strain and is subsequently stretched out. Polvani et al. (1989) also found that the onset of filamentation is associated with a stagnation point migrating inside a vortex (in their case in a two-dimensional system).

4.3 Summary and discussion

In this chapter we have studied the interaction between a vertically-propagating planetary wave front and a vertically-sheared zonal mean flow (initially free of any relevant critical levels). The quasi-linear, slowly-varying theory which we have developed shows that if the zonal mean wind decelerates by less than roughly one-half its initial value a steady state will ensue. On the other hand if the deceleration exceeds one-half its initial value no steady state is obtained. Numerical simulations with our CD/CS model shows that despite the simplifying assumptions of the theory (e.g. quasi-linearity, etc) the prediction of a one-half threshold is a very good one. The numerical model also shows that when the threshold is exceeded wave breaking eventually occurs in the shear region through a process involving the migration of a stagnation point across the vortex edge.

It is worthwhile emphasising that in our theoretical analysis we have made several simplifying assumptions, beyond quasi-linearity and slow-variation. These include the assumptions that: 1) the radial gradient of the zonally-averaged PV $\overline{q}_r$ is time-invariant; 2) the residual mean circulation is negligible and 3) the radially-integrated zonal mean flow deceleration is functionally related to the zonal mean flow deceleration at the initial vortex edge. Future work should be directed towards relaxing these assumptions in order to obtain a tighter estimate on the threshold value for wave breaking. Nonetheless, even with these apparently strong assumptions the threshold value we have derived seems a very reasonable one (at least within the range of parameters for which we have tested it).

In this Chapter we have examined a new mechanism for planetary wave breaking in a sheared zonal mean flow. We must note however that the system we have investigated is one without any non-conservative external forcing or dissipation, either of which may act to suppress the mechanism (or possibly even enhance it). Future work should be directed towards investigating the mechanism in a compressible atmosphere with the relevant external forcing agents included (e.g., radiative forcing).

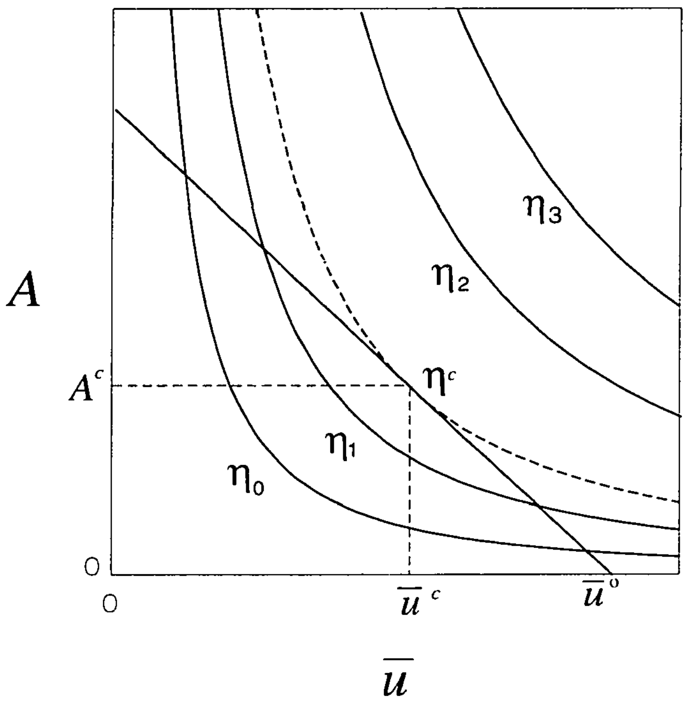

Figure 4.1: Graphical derivation of A^c and $\overline{u}^c$ as in Fyfe and Held (1990). The curves represent the relationship between A and $\overline{u}$, (based on quasi-linear slowly-varying theory) that must exist in a steady state for different forcing amplitudes η (where $\eta_0 < \eta_1 < \eta_2 < \eta_3 < \eta_4$). The straight line represents the relation between A and $\overline{u}$ that exists at all time for a flow that evolves from the initial wind $\overline{u}^\circ$. The dashed curve marks the critical amplitude η^c above which no steady states can evolve from the initial wind $\overline{u}^\circ$.

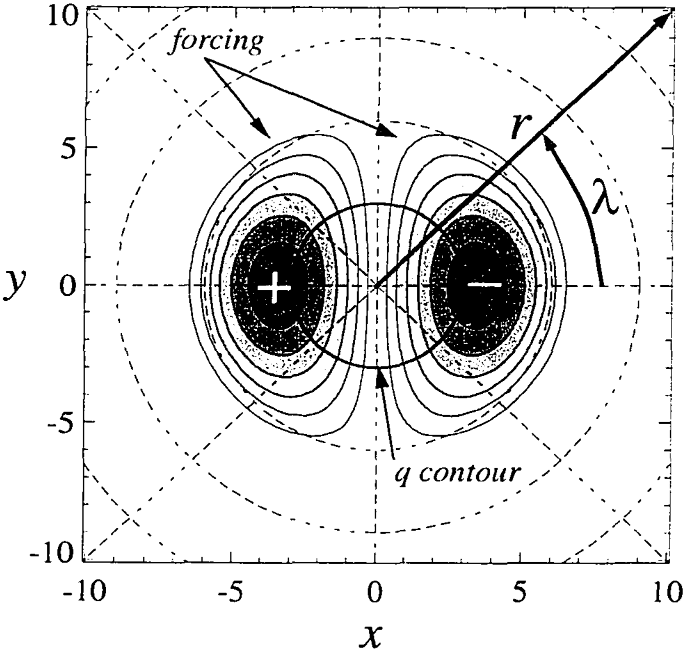

Figure 4.2: Plan view of the initial polar vortex (bold circle) on an f-cap plane. The topography is shaded. The centre of the plot is at the North Pole.

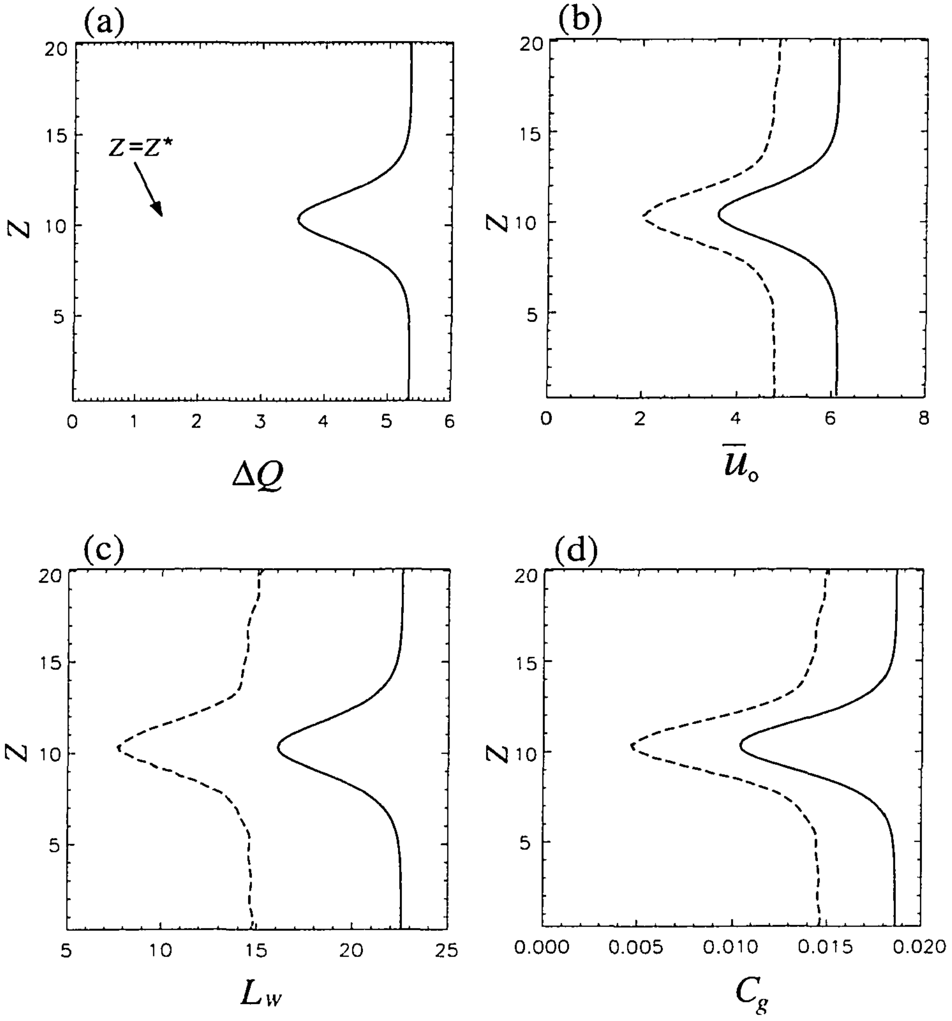

Figure 4.3: Vertical profiles of the (a) PV jump, ΔQ; (b) zonal mean flow at $r = r_o$, $\overline{u}_o$; (c) vertical wavelength, L_W and (d) vertical group velocity, C_g. The solid curves correspond to the initial state while the dashed curves were obtained diagnostically from a CD/CS simulation ($\eta_o = 0.12$) evaluated at $t = 100$.

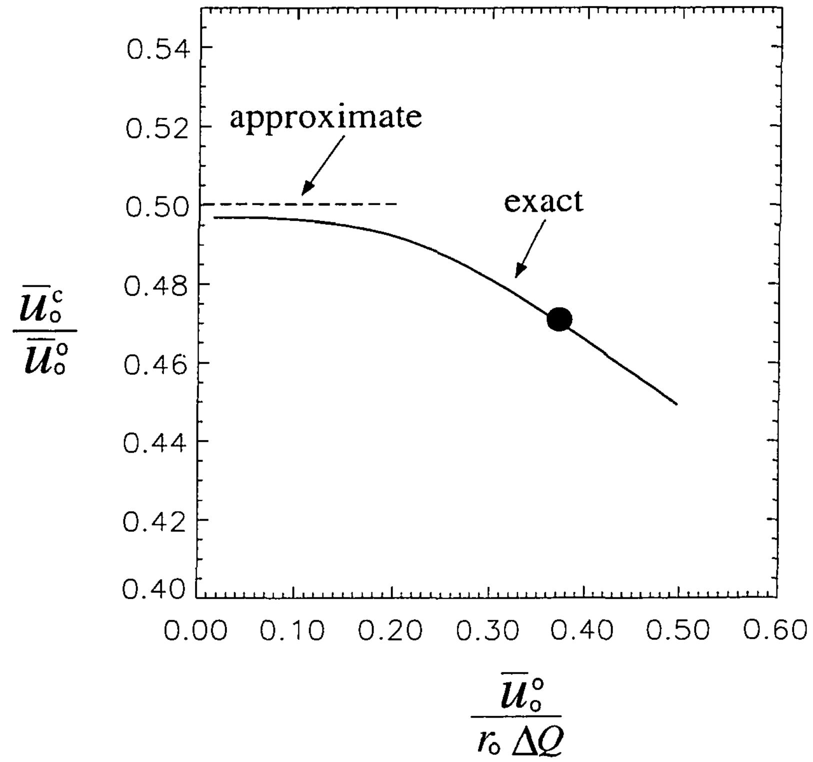

Figure 4.4: Relation between the initial state as expressed by $\overline{u}_o^o/(r_o \Delta Q)$ and the critical ratio $\overline{u}_o^c/\overline{u}_o^o$. The dashed horizontal line is the approximate ratio for small $\overline{u}_o^o/(r_o \Delta Q)$. No propagating wave solutions exist beyond $\overline{u}_o^o/(r_o \Delta Q) = 0.5$ (shaded area). The solid dot identifies the initial setup and critical ratio at Z^* in the numerical experiments discussed in Section 4.2.

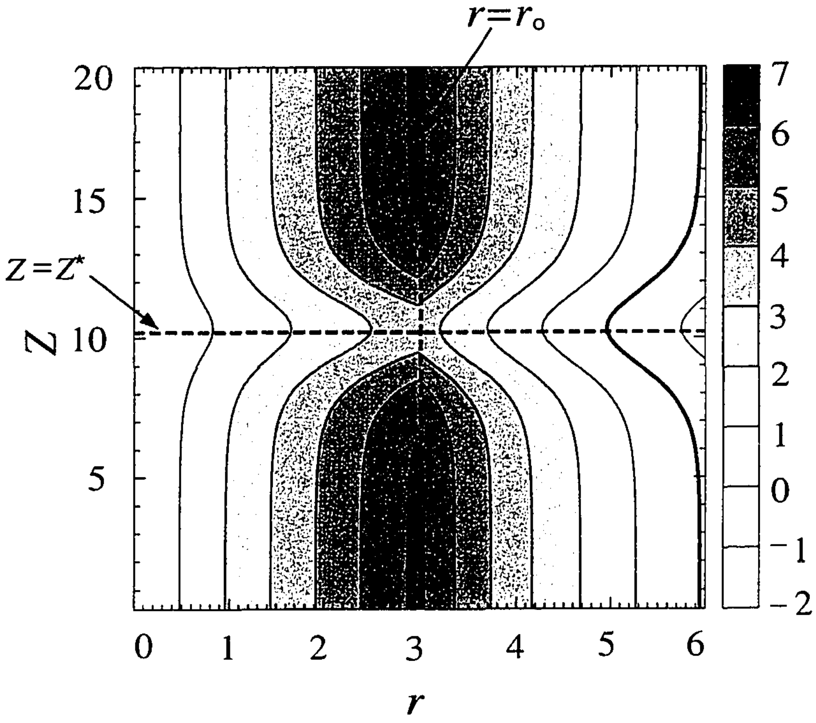

Figure 4.5: The initial zonal mean wind distribution. The zero wind line is indicated by the thick contour.

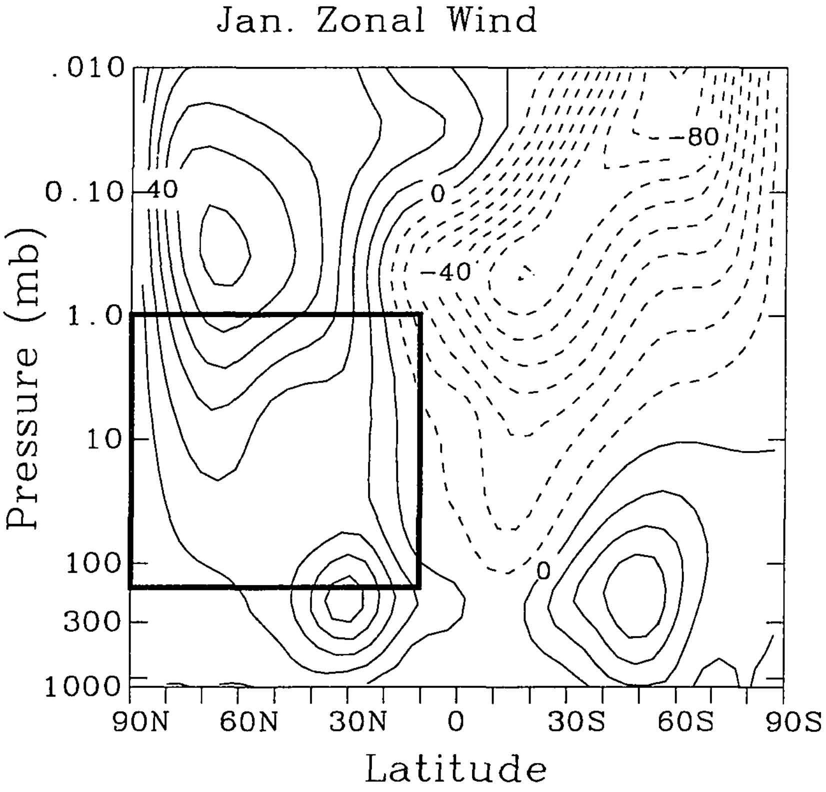

Figure 4.6: Zonally averaged zonal wind field calculated from a 3-year run with the Canadian Middle Atmosphere Model. Contour interval is 10 m/s (Beagley et al., 1997).

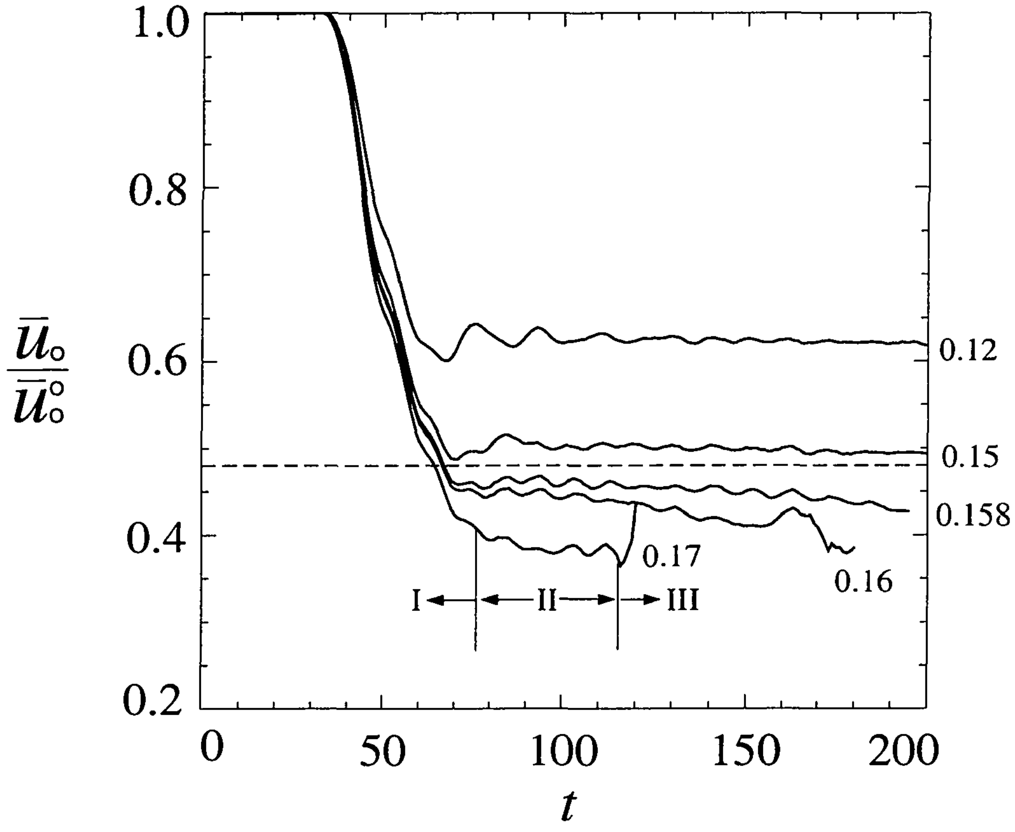

Figure 4.7: $\overline{u}_o/\overline{u}_o^o$ evaluated at Z^* for η_o=0.12, 0.15, 0.158, 0.16, 0.17. The dashed line is the critical ratio as predicted theoretically.

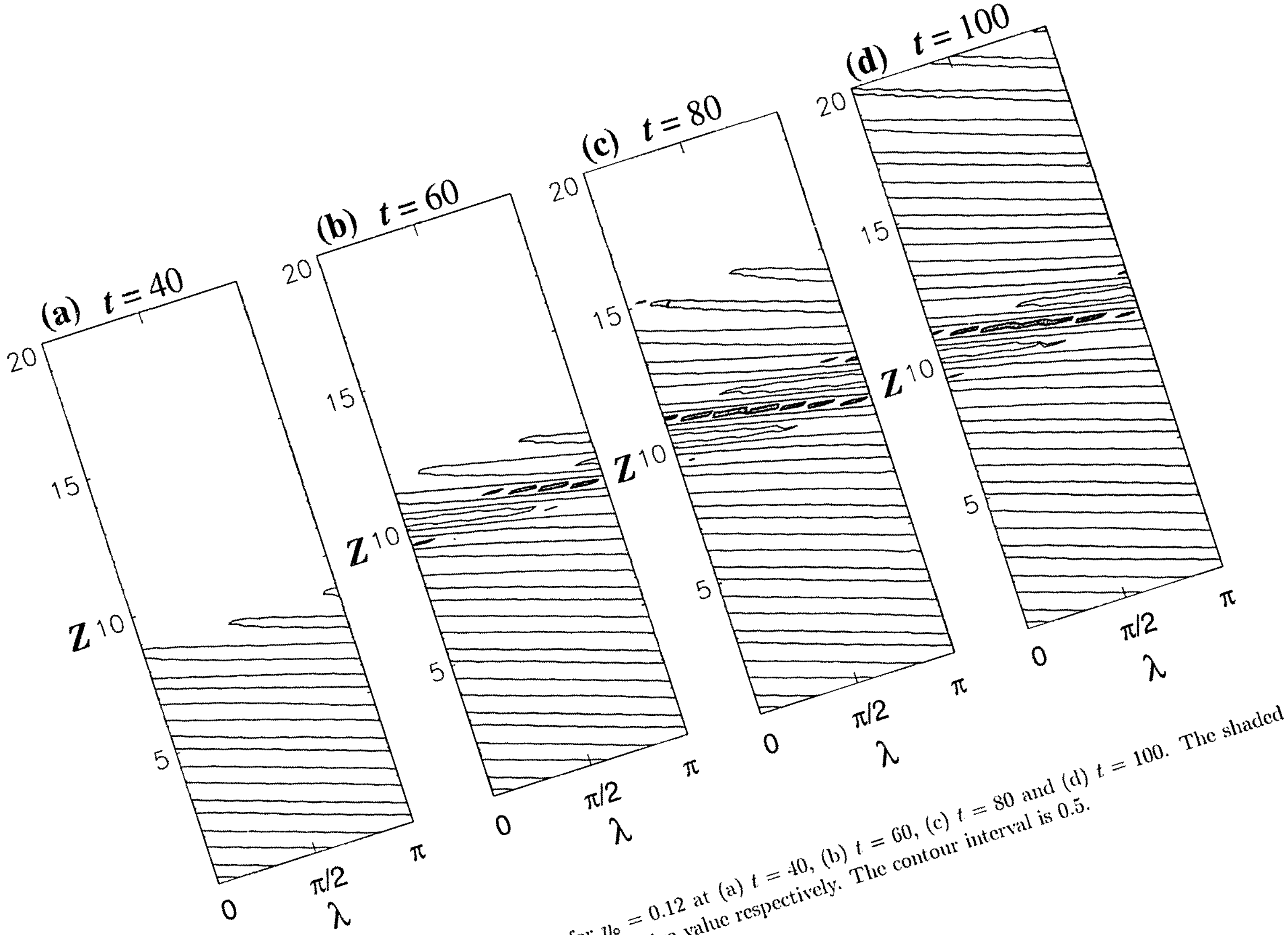

Figure 4.8: Particle displacement contour for $\eta_o = 0.12$ at (a) $t = 40$, (b) $t = 60$, (c) $t = 80$ and (d) $t = 100$. The shaded and unshaded contour represent positive and negative value respectively. The contour interval is 0.5.

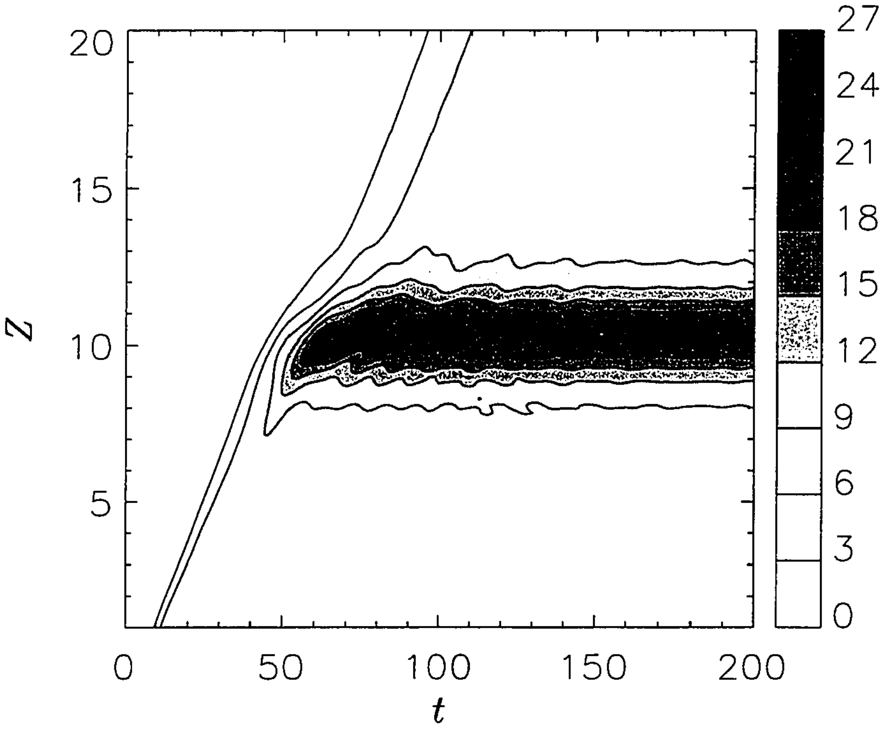

Figure 4.9: Wave activity density A (normalized by η_o^2) for $\eta_o = 0.12$.

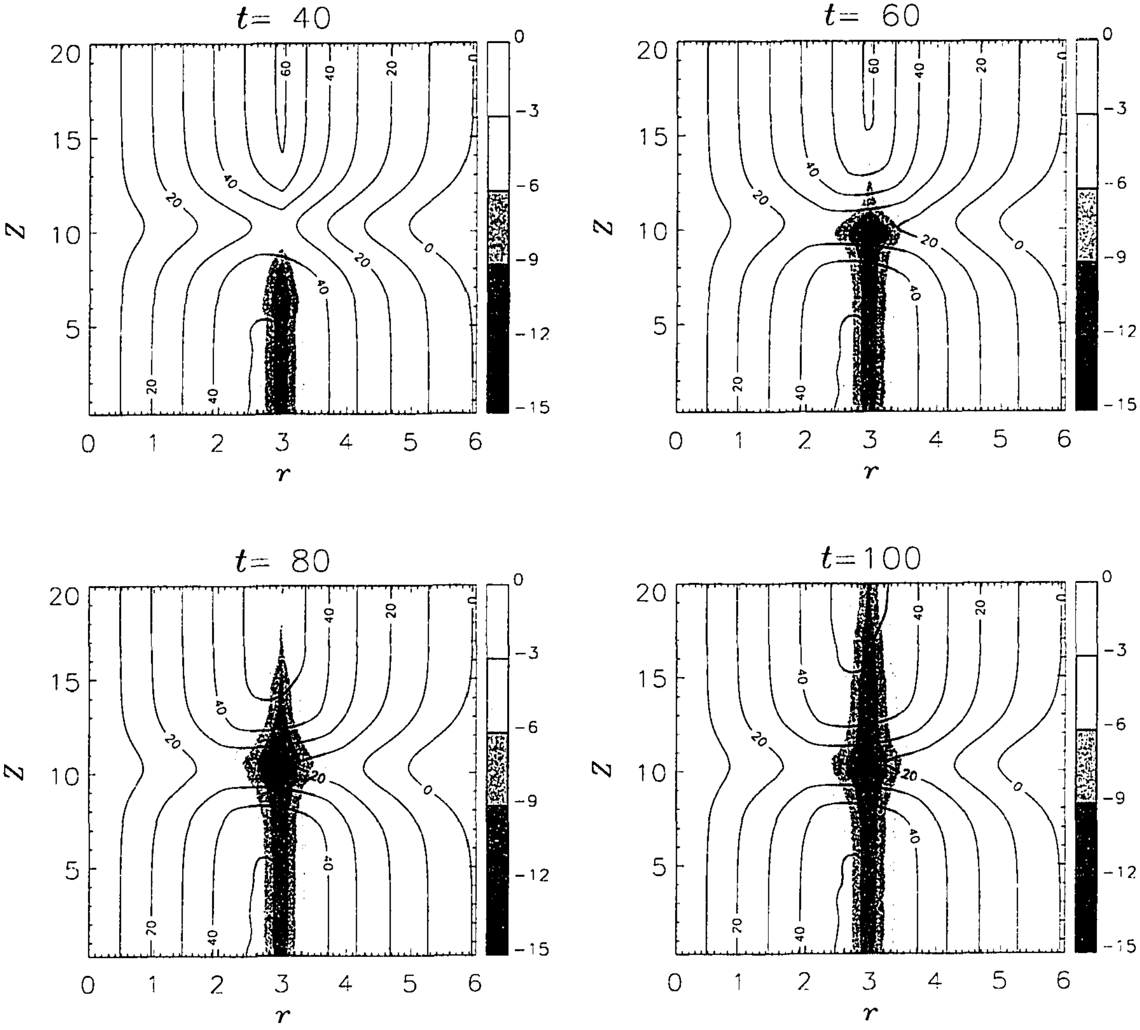

Figure 4.10: Zonal mean wind (contours) and its change (shaded) for $\eta_o = 0.12$ at t =40, 60, 80 and 100.

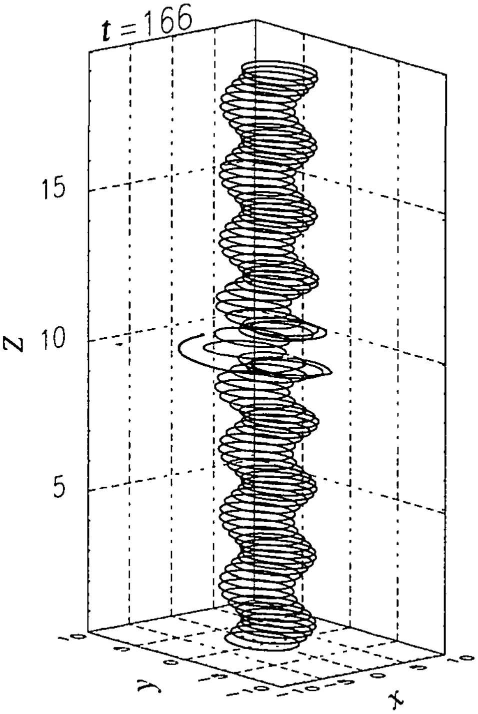

Figure 4.11: Perspective view of the vortex at $t = 166$ for η_o=0.16.

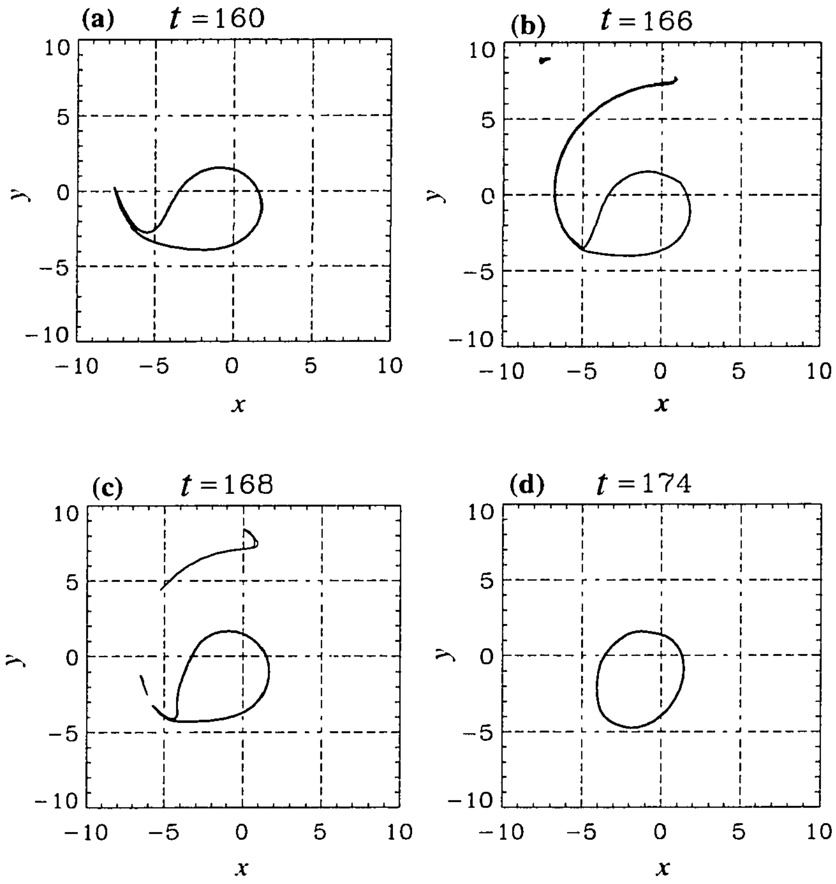

Figure 4.12: PV contour at Z^* for $\eta_o = 0.16$ at (a) $t = 160$; (b) $t = 166$; (c) $t = 168$; (d) $t = 174$.

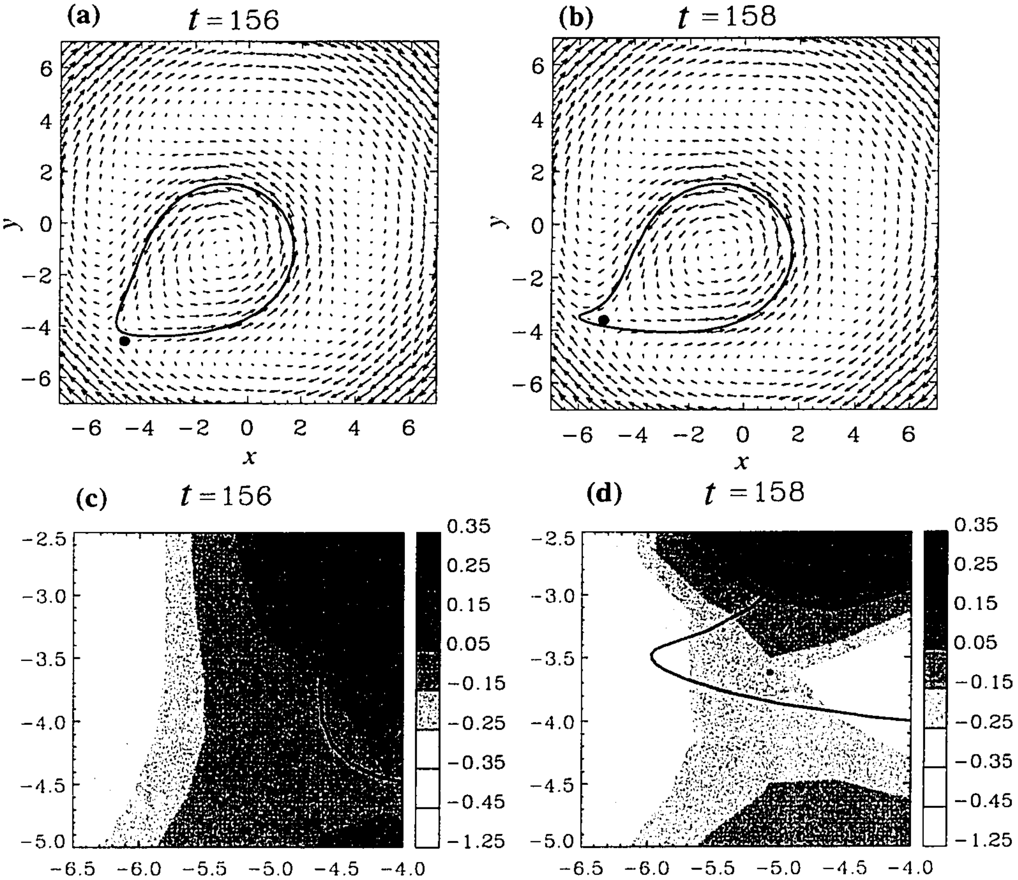

Figure 4.13: PV contour (thick and solid curve) and the stagnation point (solid dot) at Z^* for $\eta_o = 0.16$ at $t = 156$ [(a) and (c)] and $t = 158$ [(b) and (d)]. Arrows in (a) and (b) represent the velocity field. Shaded contours in (c) and (d) represent the strain field around the stagnation point.

Chapter 5

Conclusions

This study has been concerned with the breakdown of vertically-propagating planetary waves. Wave breaking is generally characterized by irreversible deformation of material contours such as potential vorticity and is a very effective means whereby waves cause the systematic redistribution not only of potential vorticity, but also of pollutants, angular momentum and other dynamical and chemical quantities of interest in atmospheric sciences. As discussed in the Introduction, planetary wave breaking is also linked to the erosion of the stratospheric polar vortex during episodes of stratospheric sudden warming. Towards improving our understanding of planetary wave breaking, and hopefully also stratospheric sudden warmings, we have set the following objectives for this study: 1) the implementation of a vertical absorbing sponge in an ultra-high resolution contour dynamics model of the stratosphere and 2) the development of a new theory for the breakdown of vertically-propagating planetary waves which does not rely on the presence of "critical levels" in the mean flow.

To these ends, in Chapter 2 we formulated the governing equations and described the numerical model used to solve these equations, namely the CD/CS method. The CD/CS method effectively allows for infinite horizontal resolution and is especially well-suited to the specific physical problem addressed here, namely, planetary wave breaking associated with the polar stratospheric vortex. The CD/CS model used was originally developed by DS for their study of the response of a barotropic vortex to topographic forcing and was modified here to include an upper absorbing sponge. The implementation of an absorbing sponge in a CD/CS model is a difficult problem owing to the conservation constraints the techniques of CD/CS impose. We believe that our implementation is the first of its kind.

Given the model described in Chapter 2, in Chapter 3 we considered the influence of the upper boundary on wave breaking in a Boussinesq environment. Here we compared CD/CS simulations using: 1) a rigid upper-boundary condition (following DS) and 2) a vertical sponge (preventing spurious reflection of upward propagating waves). In 1) both local (to the forcing) and remote breaking were evidenced for weak forcing while only local breaking was observed for sufficiently strong forcing. In 2) remote breaking was absent and local breaking, which occurs for sufficiently strong forcing, has quite a different character to that seen in 1). Compressibility effects were also discussed. While many studies exist which consider the role of upper boundaries on linear wave propagation (Lindzen et al., 1968; Beaudoin and Derome, 1976; Kirkwood and Derome, 1977) we believe this is the first to consider their role on wave breaking. Most of the results from Chapter 3 have been published in Fyfe and Wang (1997).

In Chapter 4 we investigated a new mechanism for the breakdown of vertically-propagating planetary waves. This mechanism, not unlike that exposed by FH for the case of horizontally-propagating Rossby waves, involves wave-mean interactions which under certain conditions lead to positive group-velocity/mean-flow feedbacks which in turn cause planetary wave breaking. Theoretical considerations estimate that wave breaking will occur when the zonal mean flow is decelerated by more than one-half its initial value, hence the so-called "one-half" rule for planetary wave breaking. The theory so developed involves the combined *assumptions of quasi-linearity and slow-variation (and several other subsidiary as*sumptions) whose limits were tested using a fully-nonlinear CD/CS model. The numerical simulations confirmed the one-half rule. Even with these apparently strong assumptions the threshold value we have derived seems a very reasonable one. Our numerical experiments also revealed the detailed sequence of events leading to wave breaking (which were seen to involve the migration of a stagnation point across the vortex edge).

Future work should however be directed towards relaxing the assumptions we have made to obtain a tighter estimate on the threshold value for wave breaking. Future work is also required to investigate the mechanism in a compressible atmosphere with the relevant external forcing agents included (e.g., radiative forcing).

Bibliography

[1] Andrews, D.G., J.R. Holton, and C.B. Leovy, 1987: *Middle atmosphere dynamics*. Academic Press, 489 pp.

[2] Andrews, D.G. and M.E. McIntyre, 1976: Planetary waves in horizontal and vertical shear: the generalized Eliassen-Palm relation and the mean zonal acceleration. *J. Atmos. Sci.*, *33*(11), 2031–2048.

[3] Baldwin, M.P., and J.R. Holton, 1988: Climatology of the stratospheric polar vortex and planetary wave breaking. *J. Atmos. Sci.*, *45*, 1123–1142.

[4] Barnett, J.J., 1975: Large sudden warming in the Southern Hemisphere. *Nature*, *255*, 387-389.

[5] Beagley, S.R., J. de Grandpré, J.N. Koshyk, N.A. McFarlane and T.G. Shepherd, 1997: Radiative-dynamical climatology of the first-generation Canadian middle atmosphere model. *Atmosphere-Ocean*, *35*(3), 293-331.

[6] Beaudoin, C., and J. Derome, 1976: On the modelling of stationary planetary waves. *Atmosphere*, *14*, 245–253.

[7] Boyce, W.E., and R.C. DiPrima, 1986: *Elementary differential equations and boundary value problems*. John Wiley & Sons, 680 pp.

[8] Charney, J.G., and A. Eliassen, 1949: A numerical method for predicting the perturbations of the middle latitude westerlies. *Tellus*, *1*, 38-54.

[9] Clough, S.A., N.S. Graham, and A. O'Neill, 1985: Potential vorticity in the stratosphere derived using data from satellites. *Q. J. R. Meteorol. Soc.*, *111*, 335–358.

[10] Derome, J., and A. Wiin-Nielsen, 1971: The response of a middle-latitude model atmosphere to forcing by topography and stationary heat sources. *Mon. Wea. Rev.*, *99*, 564-576.

[11] Dickinson R.E., 1970: Development of a Rossby wave critical level. *J. Atmos. Sci.*, *27*, 627–633.

[12] Dritschel, D.G., 1988: Contour Surgery: a topological reconnection scheme for extended integrations using Contour Dynamics. *J. Comput. Phys.*, *77*, 240–266.

[13] Dritschel, D.G., 1989: Contour Dynamics and Contour Surgery: numerical algorithms for extended, high-resolution modelling of vortex dynamics in two-dimensional, inviscid, incompressible flows. *Comput. Phys. Rep.*, *10*, 77-146.

[14] Dritschel, D.G., and R. Saravanan, 1994: Three-dimensional quasi-geostrophic Contour Dynamics with an application to stratospheric vortex dynamics. *Q. J. R. Meteorol. Soc.*, *120*, 1267–1297.

[15] Dunkerton T.J., 1981: Wave transience in a compressible atmosphere. Part I: transient internal wave, mean-flow interaction. *J. Atmos. Sci.*, *38*, 281–297.

[16] Dunkerton T.J., and D.P. Delisi, 1986: Evolution of potential vorticity in the winter stratosphere of January-February 1979. *J. Geophys. Res.*, *91*(D1), 1199–1208.

[17] Fyfe, J., and I.M. Held, 1990: The two-fifths and one-fifth rules for Rossby wave breaking in the WKB limit. *J. Atmos. Sci.*, *47*(6), 697–706.

[18] Fyfe, J., and X. Wang, 1997: Upper-boundary effects in a Contour Dynamics/Surgery model of the polar stratospheric vortex. *Atmosphere-Ocean*, *35*(2), 189-207.

[19] Grose, W.L., and B.J. Hoskins, 1979: On the influences of orography on large-scale atmospheric flow. *J. Atmos. Sci.*, *36*, 223–234.

[20] Juckes, M.N., 1989: A shallow water model of the winter stratosphere. *J. Atmos. Sci.*, *46*, 2934–2954.

[21] Juckes, M.N., and M.E. McIntyre, 1987: A high-resolution one-layer model of breaking planetary waves in the stratosphere. *Nature*, *328*(13), 590–596.

[22] Kalnay, E., M. Kanamitsu, R. Kistler, W. Collins, D. Deaven, L. Gandin, M. Iredell, S. Saha, G. White, J. Woollen, Y. Zhu, M. Chelliah, W. Ebisuzaki, W. Higgins, J. Janowiak, K.C. Mo, C. Ropelewski, J. Wang, A. Leetmaa, R. Reynolds, R. Jenne, and D. Joseph, 1996: The NCEP/NCAR 40-year reanalysis project. *Bull. Amer. Meteor. Soc.*, *77*, 437-471.

[23] Killworth, P.D., and M.E. McIntyre, 1985: Do Rossby-wave critical layers absorb, reflect or over reflect? *J. Fluid Mech.*, *161*, 449–492.

[24] Kirkwood, E., and J. Derome, 1977: Some effects on the upper-boundary condition and vertical resolution on modelling forced stationary planetary waves. *Mon. Wea. Rev.*, *105*, 1239-1251.

[25] Kundu, P.K., 1990: *Fluid Mechanics.* Academic Press, 638 pp.

[26] Legras, B., and D. Dritschel, 1993: A comparison of the Contour Surgery and pseudospectral methods. *J. Comput. Phys.*, *104*, 287–302.

[27] Lindzen, R.S., E.S. Batten, and J.W. Kim, 1968: Oscillations in atmospheres with tops. *Mon. Wea. Rev.*, *96*, 133-140.

[28] Nayfeh, A.H., 1981: *Introduction to perturbation techniques.* John Wiley & Sons, 519 pp.

[29] McIntyre, M.E., and T.N. Palmer, 1983: Breaking planetary waves in the stratosphere. *Nature*, *305*(13), 593-600.

[30] McIntyre, M.E., and T.N. Palmer, 1984: The "surf zone" in the stratosphere. *J. Atmos. Terr. Phys.*, *46*, 825-849.

[31] Mo, R., 1994: Studies of wave-mean interaction relevant to the middle atmospheric circulation. *Ph.D Dissertation.* University of Cambridge. 181 pp.

[32] Norton, W., 1994: Breaking Rossby waves in a model stratosphere diagnosed by a vortex-following coordinate system and a technique for advecting material contours. *J. Atmos. Sci.*, *51*(4), 654-673.

[33] Pedlosky, J., 1987: *Geophysical Fluid Dynamics.* Springer-Verlag, 710 pp.

[34] Polvani, L.M., N.J. Zabusky, and G.R. Flierl, 1989: Filamentation of coherent vortex structures via separatrix crossing: a quantitative estimate of onset time. *Phys. Fluids A*, *1*(2), 181-184.

[35] Polvani, L.M., and R.A. Plumb, 1992: Rossby wave breaking, microbreaking, filamentation, and secondary vortex formation: the dynamics of a perturbed vortex. *J. Atmos. Sci.*, *49*(6), 462-476.

[36] Schoeberl, M.R., 1978: Stratospheric warmings: observations and theory. *Rev. Geophys. Space Phys.*, *16*, 521-538.

[37] Swinbank, F., and A. O'Neill, 1994: A stratosphere-troposphere data assimilation system. *Mon. Wea. Rev.*, *122*, 686-702.

[38] Tung, K.K., and R.S. Lindzen, 1979: A theory of stationary long waves. Part II: resonant Rossby waves in the presence of realistic vertical shears. *Mon. Wea. Rev.*, *107*, 735-750.

[39] Wang, X., and J. Fyfe, 1998: Onset of planetary wave breaking in a model of the polar stratospheric vortex. *Submitted.*

[40] Warn, T., and H. Warn, 1976: On the development of a Rossby wave critical level. *J. Atmos. Sci.*, *33*, 2021-2024.

[41] Warn, T., and H. Warn, 1978: The evolution of a nonlinear critical level. *Stud. Appl. Math.*, *59*, 37-71.

[42] Watson, G.N., 1944: *A treatise on the theory of Bessel functions*, (3rd ed.). Cambridge University Press, 804 pp.

[43] Waugh, D.W., 1993: Contour Surgery simulations of a forced polar vortex. *J. Atmos. Sci.*, *50*(5), 714-730.

[44] Yih, C.S., 1980: *Stratified flows.* Academic Press, 418 pp.

[45] Zabusky, N.J., M.H. Hughes, and K.V. Roberts, 1979: Contour Dynamics for the Euler equations in two dimensions. *J. Comput. Phys.*, *30*, 96-106.

[46] Zabusky, N.J., and E.A. Overman II, 1983: Regularization of Contour Dynamical algorithms: I. tangential regularization. *J. Comput. Phys.*, *52*, 351-373.

Appendix A

Wave activity

As discussed in DS the wave activity density for a single contour per vertical level case is given by

$$A(z,t) = \frac{1}{4}\rho_\circ \Delta Q \oint_C \left(r^2 - r_\circ^2\right)^2 d\lambda,$$

under the assumption that the contours are not displaced over the Pole (as is always true in this study). Using $\eta' \equiv r - r_\circ$ the integrand can be written as $4r_\circ^2\eta'^2 + 4r_\circ\eta'^3 + \eta'^4$ which under the assumption of small particle displacements can be approximated by $4r_\circ^2\eta'^2$. Therefore, given small particle displacements we have that

$$A(z,t) \approx \rho_\circ r_\circ^2 \Delta Q \oint_C \eta'^2 d\lambda \quad = \quad 2\pi\rho_\circ r_\circ^2 \Delta Q \overline{\eta'^2}|_{r_\circ}.$$

Appendix B

Integrated PV flux

Here we derive

$$\int_0^\infty \overline{v'q'}dr = \Delta Q \overline{v'\eta'}|_{r_\circ}. \tag{B.1}$$

Some preliminaries

Substituting our plane wave solution into the linearized vorticity equation and using the piecewise-uniform definition of $\overline{q}^\circ$ yields

$$q' = \frac{s\psi'}{\overline{u}s - \sigma r}\frac{\partial \overline{q}^\circ}{\partial r} = -\frac{\Delta Q s\psi'}{\overline{u}s - \sigma r}\delta(r - r_\circ). \tag{B.2}$$

Now, for arbitrary function $F = \tilde{F}(r,z)e^{i(s\lambda - \sigma t)}$ where $\tilde{F}$ is defined for all r and z and is continuous in the interval $r_\circ - \epsilon < r < r_\circ + \epsilon$ we have that

$$\lim_{\epsilon \to 0}\int_{r_\circ - \epsilon}^{r_\circ + \epsilon} F dr = 0 \quad \text{and} \quad \int_0^\infty F q' dr = F|_{r_\circ}\int_0^\infty q' dr. \tag{B.3}$$

The first equation follows from the mean value theorem for integrals and the second from the "sifting property" of the δ-function. In what follows we implicitly use these results repeatedly, recognizing that ψ' and its derivatives with respect to λ and z are continuous and $\partial\psi'/\partial r$ is a finite function at r_o.

Main derivation

We have that

$$\int_0^\infty \overline{v'q'}dr = \frac{1}{2\pi}\int_0^{2\pi}\int_0^\infty v'q'drd\lambda = \frac{1}{2\pi}\int_0^{2\pi} v'|_{r_o}\int_0^\infty q'drd\lambda. \qquad \text{(B.4)}$$

Analyzing the q' integral further, yields

$$\begin{aligned}
\int_0^\infty q'dr &= \lim_{\epsilon\to 0}\int_{r_o-\epsilon}^{r_o+\epsilon} q'dr \\
&= \lim_{\epsilon\to 0}\int_{r_o-\epsilon}^{r_o+\epsilon}\left[\frac{1}{r}\frac{\partial}{\partial r}\left(r\frac{\partial\psi'}{\partial r}\right) + \frac{1}{r^2}\frac{\partial^2\psi'}{\partial\lambda^2} + \frac{1}{B}\frac{\partial^2\psi'}{\partial z^2}\right]dr \\
&= \lim_{\epsilon\to 0}\int_{r_o-\epsilon}^{r_o+\epsilon}\frac{1}{r}\frac{\partial}{\partial r}\left(r\frac{\partial\psi'}{\partial r}\right)dr \\
&= \frac{1}{r_o}\lim_{\epsilon\to 0}\left[\left(r\frac{\partial\psi'}{\partial r}\right)\Big|_{r_o+\epsilon} - \left(r\frac{\partial\psi'}{\partial r}\right)\Big|_{r_o-\epsilon}\right] \\
&= \left[\frac{\partial\psi'}{\partial r}\right]_{r_o^-}^{r_o^+}.
\end{aligned}$$

Applying $\lim_{\epsilon\to 0}\int_{r_o-\epsilon}^{r_o+\epsilon} dr$ to the linearized vorticity equation now yields

$$\left(\frac{\partial}{\partial t} + \frac{\overline{u}_o}{r_o}\frac{\partial}{\partial\lambda}\right)\left[\frac{\partial\psi'}{\partial r}\right]_{r_o^-}^{r_o^+} - \Delta Q v'|_{r_o} = 0, \qquad \text{(B.5)}$$

which together with the particle displacement equation produces

$$\left(\frac{\partial}{\partial t} + \frac{\overline{u}_o}{r_o}\frac{\partial}{\partial\lambda}\right)\left\{\left[\frac{\partial\psi'}{\partial r}\right]_{r_o^-}^{r_o^+} - \Delta Q\eta'|_{r_o}\right\} = 0.$$

If the quantity in the curly brackets is zero initially it will remain so for all time so

$$\int_0^\infty q'dr = \left[\frac{\partial\psi'}{\partial r}\right]_{r_o^-}^{r_o^+} = \Delta Q\eta'|_{r_o} \qquad \text{(B.6)}$$

which together with Eq. (B.4) produces our desired result given by Eq. (B.1).

Similar to the the above procedure, we can derive

$$\int_0^\infty r^2 \overline{v'q'} dr = r_\circ^2 \Delta Q \overline{v'\eta'}|_{r_\circ}. \tag{B.7}$$

Appendix C

Zonal mean flow relationship

Here we derive an approximate relationship between the radially-integrated mean zonal flow change and the mean zonal flow change at $r_\circ$ [see Eq. (4.31)]. To do so we assume that due to the passage of a wave front the initially-circular, piecewise-uniform vortex *remains circular* with centroid located distance $\epsilon(z,t)$ from the North Pole. Numerical experimentation (not shown) reveal this to be an acceptable idealization given reasonably small (albeit finite-amplitude) displacements of the centroid. Further to this we take $q \equiv \nabla^2\psi + B^{-1}\partial^2\psi/\partial z^2 \approx \nabla^2\psi = [\partial(ru)/\partial r - \partial v/\partial\lambda]/r$. The latter allows us to write

$$\Delta\overline{u} = \frac{\Delta\Gamma}{2\pi r} \quad \text{where} \quad \Gamma \equiv \int_0^{2\pi}\int_0^r qr\,dr\,d\lambda \tag{C.1}$$

is the circulation. Using the fact that QGPV is Q_i inside and Q_o outside the contour, then at $t = 0$

$$\Gamma(r,z,0) \quad = \quad \begin{cases} Q_i\pi r^2 & \text{for } r \le r_\circ, \\ Q_i\pi r_\circ^2 + Q_o(\pi r^2 - \pi r_\circ^2) & \text{for } r > r_\circ, \end{cases} \tag{C.2}$$

while at time t

$$\Gamma(r,z,t) = \begin{cases} Q_i \pi r^2 & \text{for } r \le r_o - \epsilon, \\ Q_i a + Q_o(\pi r^2 - a) & \text{for } r_o - \epsilon < r \le r_o + \epsilon, \\ Q_i \pi r_o^2 + Q_o(\pi r^2 - \pi r_o^2) & \text{for } r > r_o + \epsilon. \end{cases} \tag{C.3}$$

Various geometrical considerations lead to the following expression for a, the area common to the initial and shifted vortices, $a = \pi r_o^2 + r^2(\beta - \beta') - \epsilon r \sin\beta$ where $\cos\beta = (r^2 + \epsilon^2 - r_o^2)/2r\epsilon$ and $\cos\beta' = (r^2 - \epsilon^2 - r_o^2)/2r_o\epsilon$. From the 1st equation in Eq. (C.1) it follows that

$$\Delta\overline{u}(r,z,t) = \begin{cases} 0 & \text{for } r \le r_o - \epsilon, \\ -\dfrac{(\pi r^2 - a)\Delta Q}{2\pi r} & \text{for } r_o - \epsilon < r \le r_o, \\ -\dfrac{(\pi r_o^2 - a)\Delta Q}{2\pi r} & \text{for } r_o < r \le r_o + \epsilon, \\ 0 & \text{for } r > r_o - \epsilon. \end{cases} \tag{C.4}$$

In Figure C.1 we plot $\Delta\overline{u}$ for various arbitrary ϵ (with $r_o = 3$ and $\Delta Q = 5.3$). As can be seen, shifting the vortex results in a maximum deceleration at $r = r_o = 3$ which increases with increasing ϵ. In Figure C.2 we plot $\int_0^\infty \Delta\overline{u} dr$ (obtained numerically) verses $\Delta\overline{u}_o$ over a range of shifting parameters ϵ and for three different values of ΔQ (again with $r_o = 3$). These ΔQ span the range of ΔQ found in Figure 4.3(a). Also shown is the best least squares fit between the two quantities. We conclude that to good approximation

$$\int_0^\infty \Delta\overline{u} dr = -\mathcal{E}(\Delta\overline{u}_o)^2, \tag{C.5}$$

where $\mathcal{E}$ is functionally related to ΔQ. We note that the precise functional dependence of $\mathcal{E}$ on ΔQ is irrelevant since $\mathcal{E}$ will be seen to drop out of the subsequent analysis.

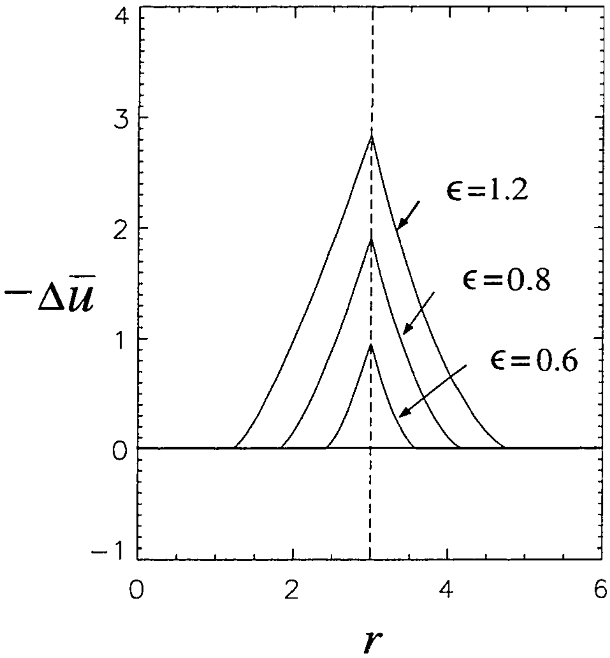

Figure C.1: The zonal mean flow change, $\Delta\overline{u}$ for $\epsilon = 0.6$, 0.8 and 1.2.

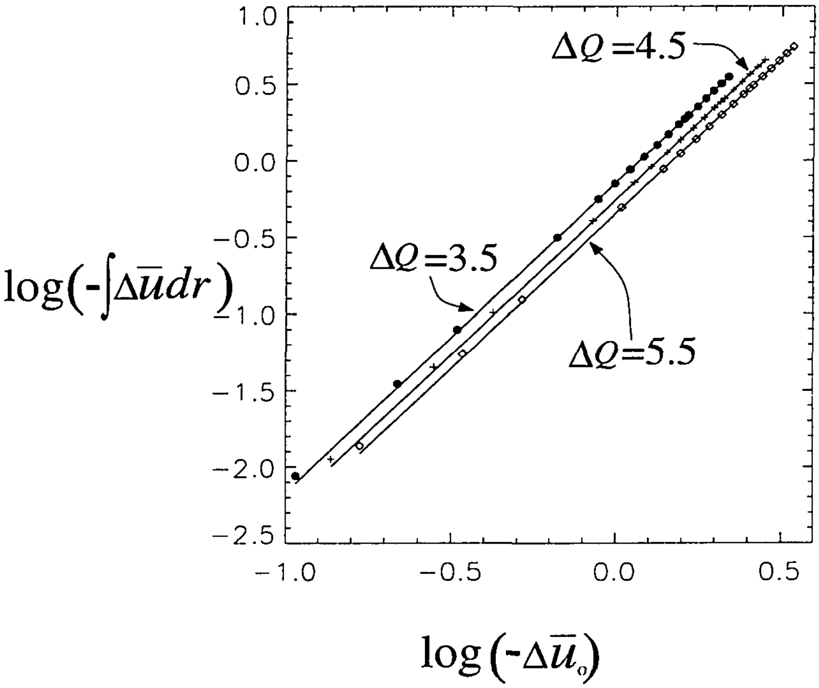

Figure C.2: Relationship between zonal mean flow deceleration at r_o, $\Delta \bar{u}_o$ and radially-integrated zonal mean flow deceleration, $\int_0^\infty \Delta \bar{u} dr$. Data points denoted by "•" corresponds to $\Delta Q = 3.5$, "+" to $\Delta Q = 4.5$ and "◇" to $\Delta Q = 5.5$. The three straight lines are the linear fits to the respective data points.

Appendix D

Steady state wave activity

Letting $x = mr_\circ/\sqrt{B}$ we have that (after considerable manipulation)

$$\begin{aligned}
\frac{\partial A}{\partial C_g} &= \frac{2\sqrt{B}A}{sr_\circ \Delta Q \left\{ I_s(x)\left[K_{s-1}(x) + K_{s+1}(x)\right] - K_s(x)\left[I_{s-1}(x) + I_{s+1}(x)\right]\right\}}, \\
\frac{\partial C_g}{\partial m} &= \frac{sr_\circ^2 \Delta Q}{2B} \left\{ \left[I_{s-1}(x) + I_{s+1}(x)\right]\left[K_{s-1}(x) + K_{s+1}(x)\right] - 2I_s(x)K_s(x) \right. \\
&\qquad \left. -0.5 I_s(x)\left[K_{s-2}(x) + K_{s+2}(x)\right] - 0.5 K_s(x)\left[I_{s-2}(x) + I_{s+2}(x)\right]\right\}, \\
\frac{\partial m}{\partial \overline{u}_\circ} &= \frac{2\sqrt{B}}{r_\circ^2 \Delta Q \left\{ \left[I_{s-1}(x) + I_{s+1}(x)\right] K_s(x) - \left[K_{s-1}(x) + K_{s+1}(x)\right] I_s(x)\right\}}.
\end{aligned}$$

Therefore

$$\frac{\partial A}{\partial \overline{u}_\circ} = \frac{\partial A}{\partial C_g}\frac{\partial C_g}{\partial m}\frac{\partial m}{\partial \overline{u}_\circ} = \frac{2A}{r_\circ \Delta Q \mathcal{D}(x)} \quad \text{where}$$

$$\begin{aligned}
\mathcal{D}(x) &= \left\{ \left[I_{s-1}(x) + I_{s+1}(x)\right] K_s(x) - I_s(x)\left[K_{s-1}(x) + K_{s+1}(x)\right]\right\}^2 / \\
&\quad \left\{ \left[I_{s-1}(x) + I_{s+1}(x)\right]\left[K_{s-1}(x) + K_{s+1}(x)\right] - 2I_s(x)K_s(x) - \right. \\
&\quad \left. 0.5 I_s(x)\left[K_{s-2}(x) + K_{s+2}(x)\right] - 0.5 K_s(x)\left[I_{s-2}(x) + I_{s+2}(x)\right] \right\}.
\end{aligned}$$